A New Global Database of Mars Impact Craters ≥1 km: 1. Database Creation, Properties, and Parameters

Stuart J. Robbins*
Laboratory for Atmospheric and Space Physics; University of Colorado at Boulder, UCB 392, Boulder, CO 80309, United States
stuart.robbins@colorado.edu
*Corresponding Author

Brian M. Hynek
Laboratory for Atmospheric and Space Physics and Department of Geological Sciences; University of Colorado at Boulder, UCB 392, Boulder, CO 80309, United States
hynek@lasp.colorado.edu

Submitted to Journal of Geophysical Research on 20 Sept. 2011
Revision, per Editors, Submitted on 10 Oct. 2011
Revision 1, Submitted 14 Jan. 2012
Revision 2, Submitted 12 Mar. 2012
Accepted 17 Mar. 2012

Total Pages - 56; Total Appendixes - 3; Total Tables - 2; Total Figures - 10.

Running Head: Mars Crater Database: Construction

Abstract:

Impact craters have been used as a standard metric for a plethora of planetary applications for many decades, including age-dating, geologic mapping and stratigraphic relationships, as tracers for surface processes, and as locations for sampling lower crust and upper mantle material. Utilizing craters for these and other investigations is significantly aided by a uniform catalog of craters across the surface of interest. Consequently, catalogs of craters have been developed for decades for the Moon and other planets. We present a new global catalog of Martian craters statistically complete to diameters $D \geq 1$ km. It contains 384,343 craters, and for each crater it lists detailed positional, interior morphologic, ejecta morphologic and morphometric, and modification state information if it could be determined. In this paper, we detail how the database was created, the different fields assigned, and statistical uncertainties and checks. In our companion paper [*Robbins and Hynek*, 2011b, this volume], we discuss the first broad science applications and results of this work.

Keywords: Mars, Mars craters, Mars crater database

Index Terms: 6225 Mars; 5420 Impact phenomena, cratering; 6055 Surfaces

43 1. Introduction

44 Since Galileo first turned his telescope to the moon and identified the three-
45 dimensionality of craters [*Galilei*, 1610], people have been cataloging craters on the solar
46 system's solid bodies. Some of the first modern crater catalogs were generated in preparation for
47 the *Apollo* missions in the 1960s with other geomorphologic features [e.g., *Kuiper*, 1960;
48 *Schimerman*, 1973], followed by more methodic and global catalogs in the subsequent decades
49 [*Pike*, 1977, 1980, 1988 and references therein; *Wood and Andersson*, 1978]. When the first
50 images of Mars were returned by *Mariner 9*, craters were cataloged there, as well. The first
51 global crater database of Mars was created by Nadine Barlow, published over two decades ago
52 [*Barlow*, 1988], and it comprised 42,284 craters, mostly with diameters $D \geq 5$ km, identifiable
53 from *Viking* images. This has stood as a reference set for the past two decades and is distributed
54 as a standard package with other Mars datasets by the United States Geological Survey (USGS).

55 Since that time, higher-quality and -resolution imagery has been gathered of Mars, as has
56 topographic data, which can be used to produce a new generation of a Mars crater catalogs.
57 Barlow is in the process of updating the "Catalog of Large Martian Impact Craters" [i.e., *Barlow*,
58 2003], which will update the locations and diameters, remove false positives, include missed
59 craters $D \geq 5$ km from the original catalog, and have several additional parameters that can be
60 calculated from recent datasets. Besides manual identification methods, automated approaches
61 have been applied to cataloging Martian impact craters. Notably, *Stepinski et al.* [2009]
62 published a catalog stated to be complete to roughly $D \sim 3$ km (see section 7.5.2). It was created
63 by purely automated machine-learning techniques utilizing the *Mars Global Surveyor*'s Mars
64 Orbiter Laser Altimeter (MOLA) data [*Zuber et al.*, 1992; *Smith et al.*, 2001]. It contains the
65 locations, diameters, and depths of all ~76,000 identified craters. An additional meta-approach
66 has been used to combine existing crater catalogs into a single database and location [*e.g.*,
67 *Salamunićcar et al.*, 2011]. This method relies upon a computer algorithm to match craters
68 across input databases and return an average location and size, subject to manual checking. This

has resulted in a database with ~129,000 craters (see Section 7.5.3).

We have created an independent Martian crater catalog with 384,343 craters complete to diameters $D \geq 1.0$ km, though we possess and will distribute the additional ~250,000 craters used to ensure this completeness on an individual basis upon request. Craters $D < 3$ km are limited to full location and size information (from Section 2), while those $D \geq 3$ km have other topographic, morphometric, and morphologic data. All craters were manually identified and measured as discussed in Section 2. The catalog also contains detailed topographic information (Section 3), interior morphology including preservation state and whether the crater is a secondary (Section 4), ejecta morphology (Section 5), and ejecta morphometry (Section 6). We discuss the completeness of the current release of this database in Section 7, and science results are laid out in our companion paper [*Robbins and Hynek*, 2011b, this volume]. Appendix A lists and describes all the parameters found in this database.

2. Crater Identification and Position, Diameter, and Ellipse Parameter Measurements

The bulk of crater identification and classification were done using THEMIS Daytime IR planet-wide mosaics [*Christensen et al.*, 2004]. The THermal EMission Imaging System (THEMIS) aboard the *2001 Mars Odyssey* NASA spacecraft is a multi-spectral thermal-infrared imager, sensitive to wavelengths between 0.42-0.86 μm and 6.8-14.9 μm. The average local time for daytime observations averages mid-afternoon to yield a high phase angle with shadows and heating effects sufficient for geomorphologic feature identification, such as craters.

In *ArcGIS* software, THEMIS Daytime IR mosaics were used to manually locate all visible craters with diameters $D \gtrsim 1$ km in approximate local coordinate systems: Most latitudes were searched in a standard Mercator cylindrical projection while those poleward of ±45-65° (varied by search) were searched in a polar stereographic projection. The THEMIS Daytime IR dataset initially used covered ~90% of the planet at 256 pix/deg resolution (230 m/pix at equator). In August 2010, the new THEMIS mosaics at 100 m/pix were used for the final stages of the database construction and all morphology characterization. Global mosaics were searched

a total of four times for craters to ensure as complete a database as possible.

Crater mapping was accomplished using *ArcGIS*'s editing tools to draw a polyline that traced the visible rim of each crater, measuring the "rim diameter" discussed in *Turtle et al*. [2005]. Polylines were created with vertex spacing of 500 m such that each representative rim ideally consists of ~$2\pi D$ vertices where D is the crater diameter. The data were all imported into *Igor Pro* software in which analysis of all polylines was completed (see Section 2.1) due to its advanced data visualization capabilities and familiarity with its built-in programming language.

The initial crater search used both THEMIS and *Viking* maps. The second search was done in the same manner except the on-screen scale was decreased to identify possible missed larger craters. The third search relied upon MOLA topographic maps at the highest resolution available (up to 1/512° per pixel at the poles (14 m/pix at 70° latitude), 1/128° per pixel equatorward of ~65-70° latitude (463 m/pix at 0° latitude)) to identify craters that may have a topographic signature but not an obvious visual one (similar to "quasi-circular depressions" [*Frey*, 2008, and references therein] though Frey does not claim that all identified features are craters as the vast majority of these have *no* corresponding feature in image data). Craters identified as depressions from MOLA data were looked at in THEMIS to determine if there was any sort of visual feature to identify it; if not, it was given a lower confidence level (see Section 4.5). From the first two searches, 286,623 craters were identified, and an additional 5,651 craters were identified with the MOLA search. While this represents an increase of only 1.97%, it represents an increase of 4.06% for craters $D \geq 5$ km, indicating that topographic data in crater identification is an important tool.

The final search was completed at significantly higher on-screen scale due to the increased fidelity of the new THEMIS Daytime IR mosaic that were used exclusively for this step. This mosaic was created in a semi-controlled fashion with estimated offsets on the order of a few hundred meters [*Edwards et al*., 2011]. The higher resolution mosaics allowed the final search to bring an estimate of the statistical completeness of the database across the entire planet to D~1.0 km (Fig. 1), even when averaged over the small regions of gaps in the imagery data

(see Section 7.1). Statistical completeness in this work is defined numerically from an incremental size-frequency plot; the diameter bin *D* greater than the diameter bin with the largest number of craters is considered to be the statistical completeness size (see Section 7.1). Due to the increased THEMIS resolution as well as the smaller crater sizes examined, the resolution at which vertices were laid down was increased by a factor of $2\times$ to 1 point every 250 meters. 75% of the planet was searched again (a fifth time) after this pass to verify completeness of the identified crater population.

Only two basins are included – Prometheus near the Martian South Pole, and Ladon near eastern Valles Marineris due to their clearly defined, if partial, rims. Other well known basins (such as Hellas or Utopia) or quasi-circular depressions [*Frey*, 2008, and references therein] were not included because their rims are more ambiguous and have been studied in much greater detail by other researchers [*e.g.*, *Schultz et al.*, 1982; *Frey and Schultz*, 1988]. Additionally, we did not include ring-shaped graben structures in highly modified polygonal terrains that some have argued are ghost craters [*e.g.*, *McGill*, 1989]. Again, we disregard this class of feature due to the ambiguity of accurate rim determinations and/or distinct evidence these features are impact craters.

2.1. Circle Fitting

All crater polylines were read into an *Igor Pro* file and fitted with a custom-written non-linear least-squares (NLLS) circle fitting routine. The algorithm employed started by converting the decimal degrees of a crater's vertices into kilometers from the center of mass (the average of all *x* values and *y* values), eliminating all first-order projection effects. The vertices were then fit with the NLLS circle algorithm that saved the best-fit center latitude and longitude as well as the circle's radius. Latitude and longitude were converted back into decimal degrees, and the radius was multiplied by 2 and saved as the diameter. Uncertainties in the fit parameters were also saved (see Section 2.3).

147 2.2. Ellipse Fitting

148 Ellipse fitting was accomplished by a stable and direct least-squares (LS) fitting
149 prescribed by *Fitzgibbon et al*. [1999] that was incorporated by the authors into *Igor Pro*. The
150 algorithm is non-iterative and does not rely upon any "guesses" for the parameters. The fit was
151 thoroughly tested and compared well with a NLLS approach though it was up to 20× faster and
152 more stable. It was used to find the major (*a*) and minor (*b*) axes, tilt angle, eccentricity *e*, and
153 ellipticity ε. Eccentricity was calculated as $e = \sqrt{1 - b^2/a^2}$ and ellipticity is defined as
154 $\varepsilon = a/b$. This is different from past approaches such as *Barlow* [1988] which determined by eye
155 which craters were elliptical and then measured those major and minor axes. A preliminary
156 analysis from these data is included in *Collins et al*. [2011].

157 2.3. Uncertainties in Circle-Fit Parameters

158 A FORTRAN95 code released as "ODRPACK95" by *Zwolak et al*. [2004] that can
159 analytically calculate uncertainties for implicit functions (functions that are not a simple function
160 *y* of *x*) is incorporated into the *Igor Pro* software. This package was incorporated into the NLLS
161 circle-fitting algorithm discussed above to calculate formal uncertainties for all circle-fit
162 parameters. The uncertainties relative to the crater diameter were plotted, and the results were
163 binned in multiplicative intervals of $2^{1/16}D$. A piece-wise power-law function (Eq. 1) describes
164 the uncertainty:

165
$$\delta D = A \cdot D^{p} \begin{cases} A = 0.017 \pm 0.004,\ p = 0.531 \pm 0.058 & ,\ 5.78 \le D \le 150 \text{ km} \\ A = 0.032 \pm 0.009,\ p = 0.121 \pm 0.250 & ,\ 1.50 \le D \le 5.78 \text{ km} \\ A = 0.023 \pm 0.004,\ p = 1.122 \pm 0.862 & ,\ 0.86 \le D \le 1.50 \text{ km} \end{cases} \quad (1)$$

166 where δD is the uncertainty in km for a given crater diameter *D* in km. This can be applied in
167 the following examples: The average fit uncertainty $\delta D(D = 1 \text{ km}) = \pm 0.02$ km (2%),
168 $\delta D(D = 10 \text{ km}) = \pm 0.06$ km (0.6%), and $\delta D(D = 50 \text{ km}) = \pm 0.14$ km (0.3%). These formal
169 uncertainties may appear somewhat small, but analytically they are the best estimates from the
170 data of what the uncertainty is *from the fit* to each crater. Additionally, analysis of several
171 craters with higher-resolution imagery resulted in very similar diameters with a general deviation

at the ~few-percent level. Examination of these relative to the power-law of the mean of a Gaussian uncertainty in the circle fits from Section 2.4 suggests similar values at small diameters, but values closer to ~1% for $D > 10$ km. These are about an order of magnitude smaller than the quoted uncertainty in the *Barlow* [1988] database of ~±10%.

2.4. Uncertainties in Crater Measurements

Because every crater was traced by hand and not by a uniformly biased computer algorithm, there was a certain amount of random uncertainty inherent in every vertex identified. At a basic level, an uncertainty of ±0.5 pix was present based upon the limits of the data even if crater rim-tracing was perfect (at the equator, ~115 m in the first two searches, ~233 m for the third, and ~50 m for the final). There was additional human error in the accuracy of each tracing that is described in brief below and detailed in Appendix B.

The human error followed a Gaussian distribution about the true rim for a crater of a given size as measured by the residuals from numerous crater fits. The standard deviation of the Gaussian varied with crater size and was well represented by a power-law (discussed in Appendix B). To understand the effects of this on the final crater database, a perfect circle of different diameters was modeled. To the x and y value of each vertex, random noise drawn from the Gaussian distribution was added where the standard deviation was given by the power-law. A Monte Carlo set of simulations both fitting a NLLS circle and LS ellipse to the model crater was run. The mean and standard deviation of each simulation set of circle diameters were recorded and plotted against the true diameter (Fig. 2, top panel). A very small aliasing of 0.4% was present at the smallest diameters, though this is an over-estimate for most of the small craters since the majority of $D \sim 1$ km craters were identified in the final search at higher resolution.

Fits to smaller craters' ellipticity ε were significantly different from their true values (Fig. 2, bottom panel) as expected based on the following thought experiment: A 1.0-km-diameter crater will have approximately 6 vertices and be 5 pixels across. If one of those vertices is 1

198 pixel "outside" of the true circle, while another is 1 pixel "inside," a ~6 by 4-pix ellipse results
199 with $\varepsilon = 1.5$; it will be less if the offsets are not two vertices apart. Therefore, it is incredibly
200 "easy" to get large ellipticities from such small craters due to very small errors in tracing.
201 An alternative way of presenting these data is how likely the ellipse fit resulting in a
202 value ε is a true representation of that value for a stated *a priori* confidence level. This can be
203 done by calculating a cumulative probability distribution as a function of diameter from the
204 Monte Carlo simulations. The ε value at which the fraction of simulations is equal to the
205 confidence level is then determined. This was graphed for 68.3%, 86.6%, 95.4%, and 99.7%
206 confidence levels in Fig. 3 (corresponding to 1, 1.5, 2, and 3σ in a Gaussian distribution). From
207 this Figure, a crater diameter must be D > 2.1 km for the confidence to be 68.3% that a derived
208 $\varepsilon < 1.1$ is a true reflection of the crater. D > 3.9 km, >5.8 km, and >8.3 km are the requisite
209 diameters for the 86.6%, 95.4%, and 99.7% confidence levels, respectively. For the noise model
210 representing the fourth search for craters, within which most smaller than ~1.5-2 km were found,
211 the values for $\varepsilon < 1.1$ are D > 1.6 km, >4.2 km, >6.2 km, and >9.2 km, respectively.

212 3. Determining Crater Topographic Properties

213 Besides basic position and diameter, one of the remaining basic parameters that describe
214 craters is depth. Only in the past decade has widespread planetary topography been available for
215 Mars, making a uniform derivation of rim heights, surface elevation, and crater floor depth
216 possible [*Smith et al*., 2001]. The *Stepinski et al.* [2009] catalog includes depth information from
217 an automated method, while that information was derived manually for this catalog and is being
218 manually derived for Barlow's revised catalog (pers. comm.).
219 MOLA gridded data were used for this analysis [*Zuber et al*., 1992; *Smith et al*., 2001].
220 The instrument operated by measuring the light-time-return of a 1.064 μm laser pulse sent from
221 *Mars Global Surveyor*, reflected off the surface, and returned to the craft. The instrument had an
222 emission rate of 10 Hz for each 8 ns pulse which, based on the average orbital speed, resulted in
223 an along-track footprint spacing of ~300 m while each footprint was ~160 m in diameter due to

spreading; inaccuracies in spacecraft orbit reconstruction result in uncertainties of ~100 m of where the footprint is centered. The across-track spacing varied significantly with latitude but was generally <2 km at the equator and much smaller closer to the poles. Vertical accuracy is ~1 m due to spacecraft orbit uncertainties [*Smith et al*., 2001]. The instrument returned approximately 595 million topographic measurements that now form its primary dataset [*Neumann et al*., 2003a, 2003b]. MOLA Experiment Gridded Data Record (MEGDR) at 1/128° per pixel scale (~463 m/pix at the equator) were used in this work.

3.1. Manual Topographic Measurements

Craters $D \geq 3$ km were measured in the MOLA data where possible. The height of the rim, elevation of the surrounding surface, and greatest depth of the crater cavity were recorded using custom-built algorithms. Manually, an *N*-dimensional polyline was created that identified points along the crater rim. A second polyline was created to identify the surface outside of the crater and its ejecta to estimate the pre-impact surface elevation; this was the most prone to uncertainty though such uncertainty is not possible to quantify because the "pre-impact surface" is open to significant interpretation. Care was taken to identify these points at least 1 crater diameter beyond the crater rim and well outside all visible ejecta and uniformly around the crater. An average of 100 points were used with a bimodal distribution peaking at $N = 41$ and 74 points. A third polyline identified the lowest points in the floor of the crater.

From these three sets, the average rim height, average surface elevation, and average crater floor depth were calculated along with the standard deviations as an estimate of the uncertainty in these measurements. The average surface value is a blind average regardless of any regional slopes. It is estimated that regional slopes will only have a potentially significant effect on craters $D > 20$ km, and on these generally only in the region of the crustal dichotomy; smaller craters may be affected by significant local slopes such as on volcanoes or the rims of larger craters. This is estimated to affect <10% of the number of craters in the database that were analyzed in this step. MOLA MEGDR count data were used to eliminate gridded points that

were an interpolation (zero actual raw data points in the MEGDR pixel). NLLS circle and ellipse fits were calculated from the rim polygons, as well, to serve as a verification of the THEMIS-based diameters (see Section 3.3 for a discussion of this comparison). The total number of points of the polygons (as well as the polygons themselves) were also saved so that: (1) A researcher may exclude from further analysis craters that had less than a certain number of points identifying, for example, the rim; (2) if different or better algorithms for determining circle or ellipse fits are created in the future, they can easily be run; and (3) it allows for spot-checking of random and outlying craters for both self-consistency and consistency between different researchers.

This step could not be done for all craters due to the coarser resolution of the MOLA gridded data compared with THEMIS. The topography of craters $D < 3$ km were not analyzed due to the inherent data limitations as discussed immediately below and in Section 7.2. Any craters $D \geq 3$ km that either (a) cannot be seen in the MOLA data, or (b) have too few non-interpolated pixels to be accurately analyzed (generally fewer than 5-10 pixels across) were also not analyzed in this step.

3.2. Using Gridded Versus Spot MOLA Topography Data (MEGDR vs. PEDR)

The accuracy of MOLA gridded data versus the point/spot data (PEDR) was examined. A nearest-neighbor search using the saved polylines from the MEGDR topographic analysis was performed for the closest PEDR point that matched a polyline vertex. An arbitrary threshold that the closest PEDR point must be within 2 gridded pixels in MEGDR was set (1/64°, or 926 meters at the equator), and the analysis was repeated with a threshold of 1 pixel with similar results. If the closest was beyond this, then the original polyline point was eliminated from this test. Any duplicates were also eliminated (since two vertices could have the same closest PEDR point). With the new topography points from PEDR for the crater rim, surrounding surface, and crater floor, the same topographic analyses from section 3.1 were run. The magnitude of the difference of the means for the two rims (MEGDR and PEDR), surfaces, and floors values was

analyzed and compared with the $\mu \pm \sigma$ calculated from the MEGDR analysis. Overall, the differences were on the scale of 10s of meters which, for >95% of cases, was within one standard deviation from the original quoted MEGDR result. Given the meaning of a "standard deviation" being one would expect ~68.3% of the data to fit within it, the use of MEGDR as described above is reliable within stated uncertainties.

Some may argue that MOLA data are not practical for analyzing crater topography for diameters smaller than ~6-10 km. In some cases, this is clearly true due to two main reasons. First, simple gaps in the MOLA coverage result in interpolation that smooths the MEGDR and decreases topographic relief [e.g., *Mouginis-Mark et al.*, 2004]. However, these are usually easily avoidable because they are fairly clear when encountered. The second is more insidious: For smaller craters, on the order of 5 km, the limited spatial resolution of the MOLA instrument could result in (a) the instrument missing the deepest portions of the crater floor and (b) missing the crest of the crater rim. In either case, a subdued crater profile would be derived and there is no obvious indication from the data that this would be in err. To roughly characterize this potential offset, three pairs of craters $D \sim 5$ and ~ 20 km were selected at random longitude from around 0°, -40°, and -80° North latitude and examined with PEDR data overlaying THEMIS mosaics. An example pair is shown in Fig. 4.

The MEGDR data that were used to identify the rims in roughly half the cases were within 2 pixels of the THEMIS rim crest, a distance chosen because it is comparable to the spot size of the MOLA footprint. When eliminating the rim points that did not have a matching PEDR, the rim heights calculated were affected by ±25 m at 0°, ±20 m at -40°, and ±10 m at -80° which were all within the stated standard deviation recorded from the original MEGDR analysis. These indicate that rim heights in this database are reliable estimators given the MOLA data fidelity so long as the quoted uncertainty is respected. Future work using HRSC (High-Resolution Stereo Camera aboard *Mars Express* [*Neukum et al*., 2004; *Gwinner et al*., 2010]) digital terrain models at ~100 m/pix scale may indicate the reliability of measurements on smaller craters.

3.3. Comparing THEMIS- and MOLA-Derived Diameters

Agreement between THEMIS- and MOLA-derived crater diameters is fairly good throughout the database. In absolute terms, ≥68% of the craters are within 1 km agreement in the two measurements at all crater sizes. Considering the level the uncertainty from the NLLS circle fit to the THEMIS rims from Section 2.3, this an acceptable spread. While the offset is reasonably constant without a statistically significant trend away from ±0 (although the means are consistently >0 for $D \lesssim 30$ km), this means that the relative difference shows a distinct trend towards >100% (parity) as diameters get larger. It is well represented by the power law $D_{\mathrm{MOLA/THEMIS}} = 1.00 + 0.41 D_{\mathrm{THEMIS}}^{-1.52}$. While this is fairly minor even for D = 3 km craters (aliased to larger diameters by 5%), it is statistically an important effect to keep in mind, not just when using these for analysis but also when exploring the effects of resolution limits on relatively small features (see Section 7.5).

4. Crater Interior Morphology and Preservation State Classification

The database contains three columns of interior crater morphology: The first is the basic crater type, the second notes any features of interest in the crater walls, and the third notes features upon the crater floor. (Appendix C, Figs. 7 and 8, provides archetypal examples of morphologic types used for both interior morphology and ejecta morphology.) Additionally, there are two more columns of information for each crater that can be loosely classified as "morphology." The first is the preservation(al) state (sometimes referred to as modification or degradation state) which is how fresh or eroded the crater appears. Second is a subjective confidence measurement of how certain the authors are that the feature identified is actually an impact crater. These are explained in detail in the following subsections.

4.1. Basic Crater Types

All craters were visually inspected to determine morphology with 100 m/pix THEMIS mosaics and rare assistance from ~5-7 m/pix CTX images (ConTeXt Camera from *Mars Reconnaissance Orbiter* [*Malin et al.*, 2007]). Craters were first categorized based on simple

gravity-controlled shape and abbreviated with three letters: Simple (Smp), complex (Cpx), and basin (Bsn). Simple craters are bowl-shaped (a smooth, continuously concave crater cavity from visual inspection); complex craters are characterized by the presence of central peaks/rings, wall terraces, and/or a flat floor [*Melosh*, 1989]. The basin classification was used for any crater larger than ~500 km in diameter (there is no agreed-upon transition diameter for where a large crater becomes a basin). Differentiating between a simple and complex crater was not attempted in all cases. For example, a partially filled simple crater will have a flat floor and become fairly identical morphologically to a small pristine complex crater that originally had a flat floor; the minimum percentage of craters classified was 44% at $D \sim 6.5$ km; of $D \geq 3$ km, 77% were classified.

Additional letters were sometimes appended; in the simple-complex transition range ($5 \lesssim D \lesssim 8$ km, see *Robbins and Hynek* [2011b], this volume), the additional letters may be present without Smp or Cpx preceding them. These are based on the morphologic types identified in *Barlow and Bradley* [1990] and are used to indicate: Flat Floors (FF), Central Peaks (CPk), Central Pits (CPt), Summit Pits (SuPt), Peak-Ring (PkRg) (observed nine times), Unclassifiable/Chaotic (Unc), and "Central Mesa" (CMa) (observed nine times). In this manner, a complex crater with a summit pit will be listed as "CpxSuPt." The Unc type was used when it was not possible to identify characteristics of the original floor of the crater due to subsequent infilling or fracturing. FF craters were only indicated for the complex type. Finally, the "CpxCMa" designation, indicating a "central mesa," applied to large craters in the complex size regime that have a mesa-like central region that spans ~50% of the crater's diameter.

4.2. Crater Walls

The second interior morphology column notes any features of interest in the crater walls. In the case of multiple features, a backslash ("/") separates multiple items. Possible features identified in the database are: Terraced, Concentric (also known as "bench"), Gullies (at THEMIS resolution), and/or a channel breaching the wall along with the compass direction (e.g.,

"Channel SE" indicates a channel breaches the southeast wall; in cases where there were numerous channels, only "Channels" was indicated). If tectonic features such as graben run through the crater and its walls, this is indicated in the floor morphology section, described in Section 4.3.

Terraces and benches are formational features. Terraces occur in complex craters due to weakness in the target material that leads to fracturing circumferential to the crater rim [*Melosh*, 1989]. Concentric craters are generally small craters that have a rim, a drop to a mid-level "bench" that is fairly flat and extends over a sizeable part of the crater's radius, and then drops to a more typical crater depth for that diameter; this bench extends over the boundary in a layered target of weak (top) and strong (bottom) material before breaching the stronger material towards the center [*Melosh*, 1989]. Channels and gullies are modification features that can occur at any time after the crater has formed. The "gullies" refers to any thin, channel-like pattern that runs down the crater wall at the resolution of THEMIS. This can be simple mass wasting, or it may be due to aquifers bursting [e.g., *Malin and Edgett*, 2000] or melting from snow deposits [*Christensen*, 2003]. The "Channel" term is *only* used when the channel breaches the crater wall and the channels are many km long.

4.3. Crater Floors

Additional features of interest on the crater floor were noted in a third interior morphology column. This includes a generic "Floor Deposits" that does not presume an origin. Floor Deposits were indicated in any complex crater that did not have a uniform floor texture, was not of the other types, or clearly had a large amount of burial (this would also be reflected in the degradation/modification state). It was indicated in simple craters if the crater rim opened to the surrounding surface and was at the same elevation, or if it was not bowl-shaped.

Other possible values in this column are: Fractured, Channel(s), Dunes, Valley Deposits, Slump Deposits, Landslide Deposits, Ejecta Deposits (from an external crater), or Tectonics. Fractured indicates a highly fractured crater floor, and this is separate from Channel(s) that

designates a crater that has one or more channels running through it (there must be a visible channel through the crater, not just breaching the wall). Dunes indicates if sand dunes are present. Valley Deposits are where a channel opens into a crater and material appears to have been deposited at its mouth. Slump Deposits are floor deposits that appear to be the result of mass wasting from the crater rim and/or walls, while Landslide Deposits are a sub-class that have a specific fan-like morphology that may be fluvial in nature. Ejecta Deposits are cases where another, external crater's ejecta is within the crater of interest; if there is ejecta on the crater floor due to a crater that formed completely inside the crater in question, this was not indicated. Tectonics are cases where extensional or compressional features are present in the crater floor, such as graben or wrinkle ridges.

4.4. Determination of Crater Preservation States

There is a lengthy history of studying the degradation/modification/preservation(al) states of craters by processes of gravitational mass wasting such as landslides, aeolian deposition and erosion, and fluvial erosion [e.g., *Grant and Schultz*, 1993; *Craddock et al.*, 1997; and *Barlow*, 1995]. Historically, crater preservation states have been reduced to three or four different classes that range from ghost (craters that are almost completely buried or eroded so they are barely visible) to pristine craters (such as by Craddock and colleagues, e.g., *Craddock et al.* [1997]). A benefit of this system is that with fewer classes, there is a larger step between each class and consistency is more likely to be maintained. With high-resolution data and data types other than imagery (such as topography and thermal inertia), *Barlow* [2004] advocated for a more detailed eight-class system based on 0-18 possible "points" a crater can be assigned that scores several different parts of the crater independently. Points are scaled to give a 0-7 preservation class. This has the benefit of both utilizing disparate data to derive a preservation class and having a system closer to a continuum of preservation states.

While the *Barlow* [2004] system may be more ideal, it is not feasible given the much larger number of craters in this database and requisite manual classification. Instead, this work

uses some of the objectivity of that system, but it has been shrunk in scope to the more traditional four-class system as listed and detailed in Table 1. In this analysis, crater "Relative Depth" was based on the local depth/Diameter ratio – equatorial or polar – rather than a global average. As discussed in *Robbins and Hynek* [2011b] (this volume) and elsewhere [e.g., *Stewart and Valiant*, 2006], this is important to take into account because even pristine craters near the Martian poles (poleward of ~±40° latitude) are, overall, significantly shallower than craters closer to the equator.

All intermediate classifications in the rank and class are preserved in-house, but only the final class is included as the `PRESERVATION_STATE` column in the released crater database.

4.5. Is This a Crater?

In several cases (~2% of the total analyzed), features included in the database are somewhat ambiguous as to whether it is a crater, or if a crater, an exogenic crater (as opposed to, *e.g.*, an endogenic collapse pit crater). The database field `CONFIDENCE_IMPACT_CRATER` contains, on a scale of 1-4, the subjective probability that the feature identified is a crater. Out of the 79,723 craters $D \geq 3$ km that were morphologically classified in this release, 193 (0.24%) were listed as 1, 396 (0.50%) as 2, 702 (0.88%) as 3, and the remaining 98.38% as 4. This amount of uncertainty is well within the variance between researchers [*Lissauer et al*., 1988].

5. Crater Ejecta Morphology Classification

Fresh craters and those with light to moderate modification will display ejecta surrounding the crater rim. Throughout the literature, this has been referred to simply as "radial," and this database abbreviates it as "Rd." An additional ejecta type, cohesive layered ejecta, has detailed descriptors based on *Barlow et al.* [2000] with slight modifications. Examples of ejecta types are found in Appendix C, and a preliminary discussion of their properties is addressed in *Robbins and Hynek* [2011b], this volume.

This database contains five morphometric fields for every crater that describe ejecta if it

is present for the crater and if that column relevant. The first is NUMBER_LAYERS and if present has a value ≥1 describing the number of layers of *cohesive* ejecta (simple radial ejecta is not included in this count). The second is MORPHOLOGY_EJECTA_1. For radial ejecta, "SLERd" is in this column. For the cohesive layered ejecta, the *Barlow et al.* [2000] nomenclature is followed (detailed in Appendix C).

The third ejecta morphology field describes the overall texture of the LE blanket and it provides additional information about its edge; this is found in MORPHOLOGY_EJECTA_2 as a two- or four-letter code to indicate whether it is hummocky or smooth, and the general shape of the terminus as short lobes, broad lobes, amorphous, or splash (detailed in Appendix C).

A fourth column MORPHOLOGY_EJECTA_3 was occasionally used to describe unique shapes of ejecta blankets. These types are: Butterfly, Rectangular, Splash, Bumblebee, and Pin-Cushion. In addition to these, "Pseudo-Butterfly" and "Pseudo-Rectangular" are occasionally used. Occasionally, a binary impact will occur and the two craters overlap, their touching rims being straight between the two. In this case, there may be cohesive ejecta that appears to be squeezed between the two in which case "bumblebee" is used for both craters. Finally, even if there is no ejecta but the crater is at the head of what on Earth would be considered a sandbar, the term "Sandbar" is placed in this column of morphology.

In the three text morphology columns, a single value applies to all layers of ejecta for that crater. If there are multiple layers that have a distinct morphology, then backslashes ("/") are used to separate them with the innermost layer first, second listed second, and so on for the first two morphology columns; it is specified in the third morphology column to which layer the designation applies. If there are, for example, three layers of ejecta where the inner and middle are sinuous rampart, the outer is circular pancake, all are hummocky, the inner has "short lobes" while the middle and outer has broad lobes, and the inner is of the butterfly type, the columns would have the following information:

1. MLERS/MLERS/MLEPC
2. HuSL/HuBL/HuBL

3. Inner is Butterfly

Finally, there is a comments column `MORPHOLOGY_EJECTA_COMMENTS` that may contain additional information about the ejecta. An example that was frequently used is, "There may be a cohesive layer within the Rd ejecta."

6. Crater Ejecta Morphometry Measurement

While the morphologic crater ejecta classification is somewhat subjective, this database also contains morphometries of the cohesive layered ejecta type in all cases where this could be measured. Due to image clarity, image completeness, and indistinct contacts, it was not possible to measure all ejecta, but the authors were able to include 15,800 ejecta layers' morphometry.

6.1. Outlining Ejecta and Calculating Their Properties

Ejecta were identified in THEMIS Daytime IR global mosaics and outlined with one vertex every 500 m. A note was made in the *ArcGIS* shapefile designating the ID of the crater to which the ejecta belonged. These were imported into *Igor Pro* software along with the already processed crater rim data and, using the same algorithms as with the crater rims, the ejecta outlines were projected from decimal degrees to kilometers from the centroid after factoring in the spherical surface of Mars. For every ejecta layer, the following data were calculated and stored to the designated database columns (where `#` refers to a number between 1 and 5, inclusive):

- `LAYER_#_PERIMETER`: Perimeter of each outline (units are km).
- `LAYER_#_AREA`: Area of each outline using a standard geometric method for the area of an irregular polygon:

$$A = \frac{1}{2}\sum_{i=0}^{n-1}\left(x_i y_{i+1} - x_{i+1} y_i\right) \quad (2)$$

where n is number of vertices, x is longitude, and y is latitude. The ideal area of the crater (πr^2) is subtracted, and the final area of the ejecta is recorded (units are km^2).

- `LAYER_#_LOBATNESS`: The lobateness, Γ, is calculated (Eq. 3) (unitless) using the ejecta area before the crater's area is subtracted.

$$\Gamma = \frac{\text{area of ejecta}}{\pi\left(\text{radius of circle with equivalent area}\right)^2} \quad (3)$$

- `LAYER_#_EJECTARAD_EQUIV`: The equivalent ejecta radius (units are km) - also known as "runout distance" - is calculated as:

$$\text{runout distance} = \sqrt{A_{\text{ejecta+crater}}/\pi} - r_{\text{crater}} \quad (4)$$

- `LAYER_#_EJECTARAD_REL`: Relative equivalent ejecta radius is the runout distance divided by the crater's radius and is also known as "ejecta mobility" (unitless).

Ejecta perimeter and area are self-explanatory and are standard definitions. Ejecta lobateness is similarly a standard definition and has been used for several decades with no modification [e.g., *Kargel*, 1986]. However, it should not be confused with the *number* of flow lobes that are observed, which confusingly is also termed "lobateness" by a few researchers [e.g., *Barnouin-Jha and Schultz*, 1998]. Runout distance and its derived ejecta mobility, however, have had two different definitions. The first is the one used here and uses an average ejecta extent; it offers a characterization of the overall energy and viscosities involved [e.g., *Barlow*, 2005, 2006]. The second is the maximum extent of the ejecta to determine the absolute farthest the cohesive ejecta could flow given the impact energy available [e.g., *Mouginis-Mark*, 1979; *Costard*, 1989] (this was not calculated).

6.2. Fractal Nature and Differing Resolutions

A limitation on the utility of ejecta perimeters and lobateness is the inherent fractal nature of the shape studied and limits of resolution - both the imagery used and the frequency of vertices in the polylines created to represent them. This was first formalized in 1967 by fractal pioneer Benoît Mandelbrot who described it in terms of measuring the coastline of Britain [*Mandelbrot*, 1967]. He found a power law relationship between the length of coastline and the length of the side of a polygon to represent the coastline, but the power law exponent varied for

508 different coasts. Similarly, the non-linear problem of perimeter varies with the complexity of the
509 ejecta, and while a SLEPC ejecta may be well-represented by a single vertex every kilometer, a
510 complex SLERS may require 10 vertices in the same space to properly represent the perimeter at
511 THEMIS resolution. Similarly, 1 vertex every kilometer may work well for a SLEPC blanket
512 surrounding a 20-km-wide crater, but significant resolution artifacts would arise for a similar
513 blanket surrounding a 1-km-wide crater.

514 Several case studies were done to illustrate this dependence and its significance. For
515 smaller craters ($D \lesssim 10$ km), CTX data were used and the ejecta was defined by a polyline with
516 vertices spaced every 50 meters. Table 2 lists the craters used in this study and their properties
517 while Fig. 5 illustrates the lobateness resulting from the different resolutions (lobateness roughly
518 normalizes different crater diameters). There is not a predictable power law that can describe the
519 change in lobateness with differing resolution, crater size, ejecta type, etc. The only two
520 conclusions that can be made were apparent *a priori*, first that craters with larger lobateness
521 continue to have a larger lobateness at changing resolutions, and second that lobateness
522 decreases with decreasing resolution. The only comparisons that should be made are internal to
523 the database, and even then the ejecta morphometry should only be compared to similarly sized
524 craters (e.g., the values for a 3-km crater will not reflect actual morphometry differences relative
525 to a 100-km crater).

526 7. Database Completeness

527 Completeness of this database is at several different diameters depending upon what
528 information is being queried:

529 7.1. Identified Craters - Statistical Diameter Completeness

530 Lacking an external database complete to significantly smaller diameters, an internal
531 mechanism was required from which to gauge completeness in the regions for which there is
532 THEMIS coverage. The mosaics used cover >99% of the surface area of the planet, but there are

small regions of gores, especially in the higher northern latitudes, that lack THEMIS or comparable imagery. The statistical completeness of the database was calculated from crater size-frequency distributions: The global database was divided into 22.5°x45° latitude/longitude intervals and an incremental size-frequency distribution was generated from the craters within each bin (based on *Crater Analysis Techniques Working Group* [1979], except with multiplicative $2^{1/16}D$ intervals instead of $2^{1/2}D$ intervals; the finer resolution was a reflection of the large number of craters in the database). Completeness was defined to be the next-larger diameter bin after the diameter with the most craters within each region (Fig. 1). A key assumption is the crater population is well behaved and will continue to increase in number as sizes decrease, at least to diameters significantly smaller than those measured here. Therefore, any decrease observed is due to missing craters in the database rather than a property of the surface.

As a whole, this is a reasonable assumption as previous work has extensively shown that the crater production function increases at least to decameter scales on Mars [e.g., *Hartmann*, 2005]. Locally, this does not always hold. There are a few regions in Fig. 1 that show completeness to diameters >1.0 km. Several of these regions as well as others (75% of the planet) were searched yet again for missed craters, and though craters on the order of ~1% were identified that had not been previously, this could not account for the lower completeness level. It is therefore likely that a geophysical process has acted to remove the ~1-km crater population in these regions at times recent enough such that they have not had time to re-accumulate. In many cases, this was the formation of another large crater and emplacement of its ejecta blanket; in others, aeolian or burial processes likely played a dominant role.

This was especially the case observed around 0°N, 0°E, where several large crater rims were seen with almost no small craters at THEMIS resolution. This is the location of the *MER* (*Mars Exploration Rover*) *Opportunity* craft. In the high northern latitudes where Lomonosov and Lyot craters are (65°N, -9°E and 51°N, 29°E, respectively), these craters and their associated ejecta dominate the region and likely explain the relative paucity of ~1 km craters. They are

close to the poles and so each subregion covers less spatial area which is probably why these large craters have this significant effect. While craters will have formed since the impact, there apparently has not been enough time to accumulate enough $D \sim 1$ km craters to affect the size-frequency distribution based on this completeness criterion, and/or there is an ongoing process actively removing them.

The end result of this analysis is a global mean completeness level of $D = 0.96$ km, with a range $0.76 < D < 1.87$ km when binned at 22.5° latitude by 45° longitude. With the two outlier regions containing Lyot and Lomonosov craters removed, the mean is $D = 0.94$ km and maximum $D = 1.32$ km around the Arabia Terra region where there has been significant erosion [*Hynek and Phillips*, 2001]. The database as released contains 384,343 craters $D \geq 1.0$ km. The entire database has an additional 252,711 craters $D < 1.0$ km that were removed from this release but may be obtained by contacting the corresponding author.

7.2. Topographic Data Completeness

MOLA data resolution is significantly coarser than THEMIS Daytime IR (except near the poles), the limitations of which were addressed earlier in this paper. Because of occasional gaps that were more deleterious to smaller craters, 100% coverage was not possible. Roughly 100% of craters $D \geq 10$ km could be analyzed, below-which a steady decrease in coverage to ~80% is observed to $D = 4$ km. At smaller diameters, the decrease is precipitous.

7.3. Ejecta Morphology and Morphometry Completeness

In the current release of this database, ejecta morphology and morphometry are complete to $D \geq 3.0$ km craters ($N = 79{,}723$). The additional 304,640 craters that are $1 \leq D < 3$ km will be classified and analyzed in a future release.

7.4. Crater Morphology Completeness

In the current release of this database, interior morphologies are complete to $D \geq 3.0$ km craters ($N = 79{,}723$). The additional 304,640 craters $1 \leq D < 3$ km will be classified and

analyzed in a future release. However, there are some cases where the morphology is ambiguous, especially in determining the difference between a complex, flat-floored crater or a simple, slightly in-filled or relaxed crater in the ~5-8 km-diameter range. In these cases, the first morphology column was left blank rather than give potentially erroneous information.

Preservation state is similar and is complete for $D \geq 3$ km in this release. Secondary crater classification in the current release is only complete for a select grouping of craters analyzed in *Robbins and Hynek* [2011a, 2011c].

7.5. Comparison with *Barlow* [1988, 2003], *Stepinski et al.* [2009], and *Salamunićcar et al.* [2011] Databases

At present, there are three other completed indiscriminant global catalogs of Martian impact craters: The original from *Barlow* [1988] and her in-progress revision [*Barlow*, 2003], the automated MOLA-derived *Stepinski et al*. [2009] catalog, and a composite catalog created by correlating several other crater catalogs [*Salamunićcar et al.*, 2011] that undergoes periodic revisions and is currently in version MA130301GT. *Barlow*'s is complete to $D = 5$ km, *Stepinski et al*.'s claims completeness to $D \approx 3$ km, while *Salamunićcar et al*.'s is $D \approx 2$ km.

A detailed comparison of all craters between these three and this catalog is beyond the scope of this paper, but a first-order comparison via an overall crater size-frequency distribution from the four can be done. As shown in Fig. 6, there is generally good agreement, though over a broad range of diameters ($5 \lesssim D \lesssim 200$ km) this database has slightly more craters. This is likely due to four total searches for craters utilizing multiple datasets as well as the use of the very latest high-resolution THEMIS mosaics. When looking at each catalog, there are marked differences at small diameters.

7.5.1. *Barlow* [1988]

The original Barlow database was created with *Viking* 1:2M photomosaic hardcopy maps, and craters were measured by hand and recorded. *Viking* images on average had the same nominal resolution as THEMIS, but significant spatial variance resulted in a non-uniform image

611 set. Nevertheless, the database contained 42,284 craters including some $D < 5$ km, though it was
612 not claimed to be complete to those sizes. In light of recent data, a revised version is underway
613 [e.g., *Barlow*, 2003]. When looking at the original catalog, Fig. 6 shows that the original was
614 also not complete to $D = 5$ km. A pre-release of the northern hemisphere was supplied by
615 Barlow and compared; it is more complete than the original, but differences remain where, in
616 general, this catalog has more craters than Barlow's. However, this difference is well within the
617 $1.2-1.3\times$ difference between researchers identified by *Hartmann et al*. [1981] and *Lissauer et*
618 *al*. [1988]. Overall, there are 15,812 northern hemisphere craters $D \geq 5$ km in this catalog,
619 12,920 in *Barlow* [1988], and 14,200 in the new in prep. edition.

620 7.5.2. *Stepinski et al.* [2009]

621 The total number of craters in this catalog is 75,919. It was created through an automated
622 computer algorithm that first identifies round, symmetric topographic depressions in the MOLA
623 MEGDR 1/128° product. The next step is to select these depressions and determine whether
624 they are craters through a trained machine-learning technique. There are significantly fewer $D >$
625 100 basins identified by *Stepinski et al*. [2009] than in the catalog presented here, likely due to
626 substantial erosion and superposed features muting the topographic signal of the original crater.
627 However, this cannot explain the discrepancy around $3 < D < 7$ km where the *Stepinski et al.*
628 [2009] catalog has a sharp increase in crater size-frequency, surpassing this one at ~6 km before
629 cresting at ~4 km and decreasing below the number identified here at ~3.5 km (Fig. 6). This
630 phenomenon is likely in large part due to the aliasing and nature of the MOLA instrument and
631 data, as described in Section 3.2.

632 7.5.3. *Salamunićcar et al.* [2011]

633 The *Salamunićcar et al*. [2011] catalog and previous iterations were constructed via a
634 semi-automated technique. Previously compiled crater catalogs (including those in the previous
635 two sub-sections) were used as input. From these, the craters are correlated to determine

636 duplicates, and duplicates are averaged. Output crater candidates are manually verified and re-
637 measured if deemed incorrect. The final catalog contains all morphometric measurements from
638 the original input catalogs and so this is a true meta-catalog of impact craters. Although a
639 slightly updated version with ~2500 additional craters exists [*Salamunićcar et al*., in press], it
640 was not available at the time of this writing. The authors state that global completeness is "up to
641 ~$D \geq 2$ km," containing 85,783 craters $D \geq 2$ km (130,301 craters in total when including smaller
642 diameters). However, the catalog in this paper contains 131,160 craters $D \geq 2$ km alone, ~50%
643 more. Thus, while their regional completeness may be to that level, it is far from globally
644 complete to 2 km. In addition, it is difficult to perform a direct comparison between their catalog
645 and this one at smaller diameters because their crater diameters are frequently rounded to odd
646 values: For example, there are 2331 craters listed with diameters 4.16 km and 1300 are D =
647 2.924 km. This results in posterization on the incremental size-frequency diagram displayed as
648 Fig. 6; a cumulative diagram retains this effect and so is also inadequate for a comparison.

649 8. Conclusions and Database Availability

650 We have completed the first global Mars crater database that is statistically complete to
651 1-km-diameter craters, numbering 384,343 entries, and it will be available for public release
652 shortly. The database was manually generated by detailed examination of THEMIS Daytime IR
653 mosaics at 232 m/pix and 100 m/pix scales as well as from MOLA gridded data at 1/128° per
654 pixel (463 m/pix). It is the first to make use of global 100 m/pix THEMIS mosaics that allowed
655 us to provide unprecedented coverage. The MOLA data used for topographic analysis is the *de*
656 *facto* standard [e.g., *Mouginis-Mark et al.*, 2004; *Stepinski et al.*, 2009] and we include several
657 topographic properties along with derived products in the catalog (e.g., the rim height above the
658 surface).

659 The database contains a robust set of statistical uncertainties in basic crater properties,
660 and overall statistics and confidence intervals are described in this paper. Besides basic position,
661 size, and topographic depth information, this it has detailed morphologic and morphometric

ejecta properties, interior morphologic indicators, and modification state information for each crater (to a certain diameter limit in this release as discussed in the text) (see Appendix A for all data columns included).

Many of the catalog parameters could be considered redundant, e.g., there are several columns listing the center latitude and longitude of craters (center of circle fit from both the imagery and topography data). For this reason, we list here what we would consider the majority of users would be interested in using: Positional data (latitude, longitude) from circle fits; crater dimensions (ellipse parameters, circle-based diameters) from imagery data. We also note that the database should be considered accurate as an ensemble as discussed above, but that the accuracy in individual craters could vary.

The catalog compares well over a large range of crater diameters with other published catalogs. Analysis of this vast database is underway, as illustrated in *Robbins and Hynek* [2011b], this volume, where we illustrate global crater distributions as a baseline before examining morphologic distributions and then re-analyze the depth-to-diameter scaling laws and simple-to-complex transition. Pending review, we will be making this database freely available for download via the Mars Crater Consortium section of USGS's MRCTR server (http://webgis.wr.usgs.gov/pigwad/down/mars_crater_consortium.htm). We are also making a web-query site that allows users to download craters and features based on user-selectable fields and options that will be available at http://craters.sjrdesign.net.

682 Acknowledgements: The authors thank S.C. Werner and B. Ivanov for thorough and helpful
683 reviews. S.J. Robbins thanks his dissertation committee for feedback used to improve this work:
684 F. Bagenal, N. Barlow, B. Hynek, B. Jakosky, and N. Schneider. This work benefited from the
685 assistance of R. Haber, D. McKenzie, D. Russell, and K. Brugman. Support for this work was
686 through NASA NESSF Award NNX07AU85H and NASA Award NNX10AL65G.
687

688 References

689 Arvidson, R., and 11 colleagues, (1979), Standard techniques for presentation and analysis of
690 crater size-frequency data, *Icarus*, *37*, 467-474.

691 Barlow, N.G. (1988), Crater size-frequency distributions and a revised Martian relative
692 chronology, *Icarus*, *75*, 285-305, doi: 10.1016/0019-1035(88)90006-1.

693 Barlow, N.G. (1995), The degradation of impact craters in Maja Valles in Arabia, Mars, *J.*
694 *Geophys. Res.*, *100(E11)*, 23,307-23,316, doi: 10.1029/95JE02492.

695 Barlow, N.G. (2003) Revision of the "Catalog of Large Martian Impact Craters," *Int. Conf. on*
696 *Mars*, *6*, Abstract #3073.

697 Barlow, N.G. (2004), Martian subsurface volatile concentrations as a function of time: Clues
698 from layered ejecta craters, *Geophys. Res. Lett.*, *31*, L05703, doi:
699 10.1029/2003GL019075.

700 Barlow, N.G. (2005), A review of Martian impact crater ejecta structures and their implications
701 for target properties, in Kenkmann, T., F., Hörz, and A. Deutsch, eds. Large meteorite
702 impacts III: Geological Society of America Special paper *384*, 433-442.

703 Barlow, N.G. (2006), Impact craters in the northern hemisphere of Mars: Layered ejecta and
704 central pit characteristics, *Meteor. & Planet. Sci.*, *41(10)*, 1425-1436, doi:
705 10.1111/j.1945-5100.2006.tb00427.x.

706 Barlow, N.G., J.M., Boyce, F.M., Costard, R.A., Craddock, J.B., Garvin, S.E.H., Sakimoto, R.O.,
707 Kuzmin, D.J., Roddy, and L.A. Soderblom, (2000), Standardizing the nomenclature of
708 Martian impact crater ejecta morphologies, *J. Geophys. Res.*, *105*, E11, 26,733-26,738,
709 doi: 10.1029/2000JE001258.

710 Barlow, N.G., and T.L. Bradley (1990), Martian impact craters: Correlations of ejecta and
711 interior morphologies with diameter, latitude, and terrain, *Icarus*, *87*, 156-179.

712 Barnouin-Jha, O.S., and P.H. Schultz (1998), Lobateness of impact ejecta deposits from
713 atmospheric interactions, *J. Geophys. Res.*, *103(E11)*, 25,739-25,756, doi:
714 10.1029/98JE002025.

715 Christensen, P.R. (2003), Formation of recent Martian gullies through melting of extensive
716 water-rich snow deposits, *Nature*, *422*, 45-48, doi: 10.1038/nature01436.

717 Christensen, P.R., and 10 colleagues (2004), The Thermal Emission Imaging System (THEMIS)
718 for the Mars 2001 Odyssey Mission, *SSRv*, *110:1*, 85-130, doi:
719 10.1023/B:SPAC.0000021008.16305.94.

720 Collins, G.S., T. Davidson, D. Elbeshausen, S.J. Robbins, and B.M. Hynek (2011), The
721 relationship between impact angle and crater ellipticity, *EPSL*, *310:1-2*, 1-8, doi:
722 10.1016/j.epsl.2001.07.023.

723 Costard, F.M. (1989) The spatial distribution of the volatiles in the Martian hydrolithosphere,
724 *Earth, Moon, & Plan.*, *45*, 265-290.

725 Craddock, R.A., T.A., Maxwell, and A.D. Howard (1997), Crater morphometry and modification
726 in the Sinus Sabaeus and Margaritifer Sinus regions of Mars, *J. Geophys. Res.*, *102(E6)*,
727 13,321-13,340, doi: 10.1029/97JE01084.

728 Edwards, C.S., K.J. Nowicki, P.R. Christensen, J. Hill, N. Gorelick, and K. Murray (2011),

729 Mosaicking of global planetary image datasets: 1. Techniques and data processing for
730 Thermal Emission Imaging System (THEMIS) multi-spectral data, *J. Geophys. Res.*, *116*,
731 E10008, doi: 10.1029/2010JE003755.

732 Fitzgibbon, A., M. Pilu, and R.B. Fisher (1999), Direct least square fitting of ellipses, *IEEE*
733 *Trans. Pattern Anal. Mach. Intell.*, *21:5)*, 476-480, doi: 10.1109/34.765658.

734 Frey, H.V. (2008), Ages of very large impact basins on Mars: Implications for the late heavy
735 bombardment in the inner solar system, *Geophys. Res. Lett.*, *35*, L13203, doi:
736 10.1029/2008GL033515.

737 Frey, H.V., and R.A. Schultz (1988), Large impact basins and the mega-impact origin for the
738 crustal dichotomy on Mars, *Geophys. Res. Lett*, *15:3*, 229-232, doi:
739 10.1029/GL015i003p00229.

740 Galilei, G. (1610), Sidereus Nuncius, Venice, Italy, 1-29.

741 Grant, J.A., and P.H. Schultz (1993), Degradation of selected Terrestrial and Martian impact
742 craters, *J. Geophys. Res.*, *98(E6)*, 11,025-11,042, doi: 10.1029/93JE00121.

743 Gwinner, K., F. Scholten, F., Preusker, S., Elgner, T., Roatsch, M., Spiegel, R., Schmidt, J.,
744 Oberst, R., Jaumann, and C. Heipke (2010) Topography of Mars from global mapping by
745 HRSC high-resolution digital terrain models and orthoimages: Characteristics and
746 performance, *Earth & Plan. Sci. Lett.*, *294*, 506-519, doi: 10.1016/j.epsl.2009.11.007.

747 Hartmann, W.K. (2005), Martian cratering 8: Isochron refinement and the chronology of Mars,
748 *Icarus*, *174*, 294-320, doi: 10.1016/j.icarus.2004.11.023.

749 Hartmann, W.K., D.P., Cruikshank, J., Degewij, and R.W., Capps (1981), Surface materials on
750 unusual planetary object Chiron, *Icarus*, *47*, 333-341, doi: 10.10160019-1035(81)90181-
751 0.

752 Hynek, B.M., and R.J. Phillips (2001), Evidence for extensive denudation of the Martian
753 highlands, *Geology*, *29:5*, 407-410, doi: 10.1130/0091-
754 7613(2001)029<0407:EFEDOT>2.0.CO;2.

755 Kargel, J.S. (1986), Morphologic variations of Martian rampart crater ejecta and their
756 dependencies and implications, *Lunar Planet. Sci. Conf.*, *XVII*, 410-411.

757 Kuiper, G.P. (1960), Photographic Lunar Atlas, University of Chicago Press, Chicago.

758 Lissauer, J.J., S.W., Squyers, and W.K. Hartmann (1988), Bombardment history of the Saturn
759 system, *J. Geophys. Res.*, *93*, 13,776-13,804, doi: 10.1029/JB093iB11p13776.

760 Malin, M.C., and K.S. Edgett (2000), Evidence for recent groundwater seepage and surface
761 runoff on Mars, *Science*, *288*, 2330-2335, doi: 10.1126/science.288.5475.2330.

762 Malin, M.C., and 13 colleagues (2007), Context Camera investigation on board the Mars
763 Reconnaissance Orbiter, *J. Geophys. Res.*, *112(E5)*, doi: 10.1029/2006JE002808.

764 Mandelbrot, B. (1967), How long is the coast of Britain? Statistical self-similarity and fractional
765 dimension, *Science*, *156*, 636-639.

766 McGill, G.E. (1989), Buried topography of Utopia, Mars – Persistence of a giant impact
767 depression, *J. Geophys. Res.*, *92*, 2753-2759, doi: 10.1029/JB094iB03p02753.

768 Melosh, H.J. (1989), Impact cratering: A geologic process, Oxford University Press, New York.

769 Mouginis-Mark, P.J. (1979), Martian fluidized crater morphology: Variations with crater size,

770 latitude, altitude, and target material, *J. Geophys. Res.*, *84(B14)*, 8011-8022, doi:
771 10.1029/JB084iB14p08011.

772 Mouginis-Mark, P.J., H., Garbeil, J.M., Boyce, S.E.C., Ui, and S.M. Baloga, (2004), Geometry
773 of Martian impact craters: First results from an interactive software package, *J. Gephys.*
774 *Res.*. *109*, E08006, doi: 10.1029/2003JE002147.

775 Neukum, G., and R. Jaumann (2004), HRSC: The High Resolution Stereo Camera of Mars
776 Express, in Wilson, A., and A. Chicarro, eds., *ESA Special Publications*, *1240*, 17-35.

777 Neumann, G.A., J.B., Abshire, O., Aharonson, J.B., Garvin, X., Sun, and M.T. Zuber (2003a),
778 Mars Orbiter Laser Altimeter pulse width measurements and footprint-scale roughness,
779 *Geophys. Res. Lett.*, *30(11)*, 1561, doi: 10.1029/2003GL017048.

780 Neumann, G.A., F.G., Lemoine, D.E., Smith, and M.T. Zuber (2003b), The Mars Orbiter Laser
781 Altimeter archive: Final precision experiment data record release and status of
782 radiometry, *Lunar Planet. Sci.*, *XXXIV*, Abstract #1978.

783 Pike, R.J. (1977), Apparent depth/apparent diameter relation for lunar craters, *Proc. Lunar. Sci.*
784 *Conf.*, *8*, 3427-3436.

785 Pike, R.J. (1980), Formation of complex impact craters: Evidence from Mars and other planets,
786 *Icarus*, *43*, 1-19, doi: 10.1016/0019-1035(80)90083-4.

787 Pike, R.J. (1988), Geomorphology of impact craters on Mercury, 165-273, Chapter 8 in Vilas, F.,
788 Chapman, C.R., and Matthews, M.S., eds., 1988, Mercury, University of Arizona Press,
789 ISBN 0-8165-1085-7.

790 Robbins, S.J., and B.M. Hynek (2011a), Distant secondary craters from Lyot crater, Mars, and
791 implications for the surface ages of planetary bodies, *Geo. Res. Lett.*, *38*, L05201, doi:
792 10.1029/2010GL046450.

793 Robbins, S.J., and B.M. Hynek (2011b), A new global database of Mars impact craters ≥1 km:
794 2. Global and regional properties and variations, and their implications to surface
795 properties and gravity scaling, Submitted to *J. Geophys. Res*.

796 Robbins, S.J., and B.M. Hynek (2011c), Secondary crater fields from 24 large primary craters on
797 Mars: Insights into nearby secondary crater production, *J. Geophys. Res.*, in press, doi:
798 10.1029/2011JG003820.

799 Salamunićcar, G., S. Lončarić, and E. Mazarico (in press), LU60645GT and MA132843GT
800 catalogues of Lunar and Martian impact craters developed using a Crater Shape-based
801 interpolation crater detection algorithm for topography data, *Planet. & Space Sci.*, doi:
802 10.1016/j.pss.2011.09.003.

803 Salamunićcar, G., S. Lončarić, P., Pina, L., Bandeira, and J. Saraiva (2011), MA130301GT
804 catalogue of Martian impact craters and advanced evaluation of crater detection
805 algorithms using diverse topography and image datasets, *Planet. & Space Sci.*, *59*, 111-
806 131, doi: 10.1016/j.pss.2010.11.003.

807 Schimerman, L.A. ed. (1973), The Lunar cartographic dossier, Series NASA-CR 1464000.

808 Smith, D.E., and 23 colleagues (2001), Mars Orbiter Laser Altimeter: Experiment summary
809 after the first year of global mapping on Mars, *J. Geophys. Res.*, *106*, 23,689-23,722, doi:
810 10.1029/2000JE001364.

811 Stepinski, T.F., M.P., Mendenhall, and B.D. Bue (2009), Machine cataloging of impact craters

812 on Mars, *Icarus*, *203*, 77-87, doi: 10.1016/j.icarus.2009.04.026.

813 Stewart, S.T., and G.J. Valiant (2006), Martian subsurface properties and crater formation
814 processes inferred from fresh impact crater geometries, *Meteor. & Planet. Sci.*, *41(10)*,
815 1509-1537.

816 Turtle, E.P., E. Pierazzo, G.S. Collins, G.R. Osinski, H.J. Melosh, J.V. Morgan, and W.U.
817 Reimold (2005), Impact structures: What does crater diameter mean?, in Kenkmann, T.,
818 F. Hörz, and A. Deutsch, eds., Large meteorite impacts III, *Geological Society of*
819 *America Special Paper 384*, 1-24.

820 Wood, C.A., and L. Andersson (1978), Lunar crater morphometry: New data, *Proc. Lunar*
821 *Planet. Sci. Conf*, ***9***, 1267-1269.

822 Zuber, M.T., D.E., Smith, S.C., Solomon, D.O. Muhleman, J.W., Head, J.B., Garvin, J.B.,
823 Abshire, and J.L. Bufton (1992), The Mars Observer laser altimeter investigation, *J.*
824 *Geophys. Rev.*, *97*, 7781-7797.

825 Zwolak, J.W., P.T. Boggs, and L.T. Watson (2004), ODRPACK95: A weighted orthogonal
826 distance regression code with bound constraints, Technical Report TR-04-31, Computer
827 Science, Virginia Tech.

828

Appendix A - Columns in the Database and Brief Descriptions

This Appendix lists all columns present in the released database as well as a brief description. Text `in fixed-width font` is the column name as it appears in the database. For brevity and since many columns effectively have the same description, items [in square brackets] are multiple instances of the prefix or suffix with the text in square brackets as the variable. For example, `LATITUDE_CIRCLE_[IMAGE, TOPOG]` indicates that there are two columns in the database, one named `LATITUDE_CIRCLE_IMAGE` and the other `LATITUDE_CIRCLE_TOPOG`.

`CRATER_ID` Crater ID is of the format ##-######. The first two numbers indicate the Mars subquad (map available at http://planetarynames.wr.usgs.gov/Page/mars1to5mMOLA), while the last six are craters in order of largest to smallest diameter within that subquad. Column format is fixed-width, 9-character string.

`LATITUDE_CIRCLE_[IMAGE, TOPOG]` Latitude from the derived center of a non-linear least-squares circle fit to the vertices selected to manually identify the crater rim. Units are decimal degrees North. Column format is variable-width, signed decimal to the thousandths place.

`LONGITUDE_CIRCLE_[IMAGE, TOPOG]` Longitude from the derived center of a non-linear least-squares circle fit to the vertices selected to manually identify the crater rim. Units are decimal degrees East. Column format is variable-width, signed decimal to the thousandths place.

`LATITUDE_ELLIPSE_IMAGE` Latitude from the derived center of a non-linear least-squares ellipse fit to the vertices selected to manually identify the crater rim. Units are decimal degrees North. Column format is variable-width, signed decimal to the thousandths place.

LONGITUDE_ELLIPSE_IMAGE Longitude from the derived center of a non-linear least-squares ellipse fit to the vertices selected to manually identify the crater rim. Units are decimal degrees East. Column format is variable-width, signed decimal to the thousandths place.

DIAM_CIRCLE_[IMAGE, TOPOG] Diameter from a non-linear least-squares circle fit to the vertices selected to manually identify the crater rim. Units are km. Column format is variable-width, decimal to the hundredths place.

DIAM_ELLIPSE_MAJOR_IMAGE Major axis of a non-linear least-squares ellipse fit to the vertices selected to manually identify the crater rim. Units are km. Column format is variable-width, decimal to the hundredths place.

DIAM_ELLIPSE_MINOR_IMAGE Minor axis of a non-linear least-squares ellipse fit to the vertices selected to manually identify the crater rim. Units are km. Column format is variable-width, decimal to the hundredths place.

DIAM_ELLIPSE_ECCEN_IMAGE Eccentricity of the non-linear least-squares ellipse fit, defined as $e = \sqrt{1 - b^2/a^2}$. Column format is variable-width, decimal to the hundredths place.

DIAM_ELLIPSE_ECCEN_IMAGE Ellipticity of the non-linear least-squares ellipse fit, defined as $\varepsilon = a/b$. Column format is variable-width, decimal to the hundredths place.

DIAM_ELLIPSE_ANGLE_IMAGE Tilt angle of the non-linear least-squares ellipse fit. Units are degrees between ±90° where 0° has the major axis aligned along a line of latitude, and positive values are counter-clockwise. Column format is variable-width, signed decimal to the hundredths place.

DEPTH_RIM_TOPOG Average elevation of each of the manually determined *N* points along the crater rim. Points are selected as relative topographic highs under the assumption they are the least eroded so most original points along the rim. Units are km. Column format is variable-width, signed decimal to the hundredths place.

DEPTH_RIM_SD_TOPOG The standard deviation from the mean of the *N* points along the

rim. Units are km. Column format is variable-width, decimal to the hundredths place.

DEPTH_SURFACE_TOPOG Average elevation of each of the manually determined *N* points outside of the crater rim and any visible ejecta blanket. This is notoriously difficult to estimate due to ejecta blankets from the crater of interest and other craters, as well as other complicating topologic features. Units are km. Units are km. Column format is variable-width, signed decimal to the hundredths place.

DEPTH_SURFACE_SD_TOPOG The standard deviation from the mean of the *N* points along the rim. Units are km. Column format is variable-width, decimal to the hundredths place.

DEPTH_FLOOR_TOPOG Average elevation of each of the manually determined *N* points inside the crater floor. Points were chosen as the lowest elevation that did not include visible embedded craters. Units are km. Units are km. Column format is variable-width, signed decimal to the hundredths place.

DEPTH_FLOOR_SD_TOPOG The standard deviation from the mean of the *N* points along the rim. Units are km. Column format is variable-width, decimal to the hundredths place.

DEPTH_RIMFLOOR_TOPOG Defined as DEPTH_RIM_TOPOG - DEPTH_FLOOR_TOPOG Units are km. Column format is variable-width, signed decimal to the hundredths place.

DEPTH_RIMHEIGHT_TOPOG Defined as DEPTH_RIM_TOPOG - DEPTH_SURFACE_TOPOG Units are km. Column format is variable-width, signed decimal to the hundredths place.

DEPTH_SURFFLOOR_TOPOG Defined as DEPTH_SURFACE_TOPOG - DEPTH_FLOOR_TOPOG Units are km. Column format is variable-width, signed decimal to the hundredths place.

PTS_USED_RIM_[IMAGE, TOPOG] Number of *N* points manually selected around the crater rim to identify the crater. Units are km. Column format is variable-width, integer.

PTS_USED_SURFACE Number of *N* points manually selected around the crater's surface for the topographic analysis. Column format is variable-width, integer.

PTS_USED_FLOOR Number of *N* points manually selected within the crater's floor for the topographic analysis. Column format is variable-width, integer.

PTS_USED_LAYER_1 Number of *N* points manually selected along the perimeter of the inner-most (or only) layer of the crater's ejecta. Note that this was done with THEMIS Daytime IR mosaics. Column format is variable-width, integer.

PTS_USED_LAYER_[2, 3, 4, 5] Number of *N* points manually selected along the perimeter of each successively outer crater layer (or blank if the crater does not have those lobes). Column format is variable-width, integer.

NUMBER_LAYERS The maximum number of cohesive layers in any azimuthal direction that could be reliably identified. Column format is 1 digit integer.

MORPHOLOGY_CRATER_1 Basic morphology of the crater interior (following Barlow and Bradley, 1990); examples are illustrated in Appendix C. Column format is variable-width, string.

MORPHOLOGY_CRATER_2 Notes features of interest through or on the crater wall. Column format is variable-width, string.

MORPHOLOGY_CRATER_3 Notes features of interest on the crater floor. Column format is variable-width, string.

MORPHOLOGY_EJECTA_1 Ejecta morphology classified following Barlow *et al.*, 2000; examples are illustrated in Appendix C. If there are multiple values, separated by a "/", then the order is the inner-most ejecta through the outer-most, or the top-most through the bottom-most. Column format is variable-width, string.

MORPHOLOGY_EJECTA_2 The morphology of the layers(s) itself/themselves. This column further describes the ejecta/layer morphology to help differentiate. This classification system is unique to this work. Examples are illustrated in Appendix C. Column format is variable-width, string.

MORPHOLOGY_EJECTA_3 Overall texture and/or shape of some of the layer(s)/ejecta that are generally unique and deserve separate morphological classification. Examples are illustrated in Appendix C. Column format is variable-width, string.

MORPHOLOGY_EJECTA_COMMENTS Notes or comments about the ejecta or possible ejecta if it was ambiguous. Column format is variable-width, string.

PRESERVATION_STATE An integer 1-4 that describes how fresh or degraded a crater is. Values are defined in Section 4.4. Column format is 1-digit integer.

CONFIDENCE_IMPACT_CRATER In some cases, a partial circular depression was identified as a crater, but we are not certain it is a crater. This column is a subjective certainty from 1-4 that the crater is really a crater (1 would be not very confident, 2 is equal chance it may or may not be, 3 is that it very likely is an impact crater, and 4 would be a definite crater). Column format is 1-digit integer.

LAYER_[1, 2, 3, 4, 5]_PERIMETER Perimeter of the manually determined *N*-dimensional irregular polyline of the layer. Units are km. Column format is variable-width, decimal to the hundredths place.

LAYER_[1, 2, 3, 4, 5]_AREA Area of the manually determined *N*-dimensional irregular polyline of the layer. This is with the area within the crater's rim removed. Units are km^2. Column format is variable-width, decimal to the hundredths place.

LAYER_[1, 2, 3, 4, 5]_LOBATENESS Abbreviated as Γ. Gives a measure of the lobateness (Bridges and Barlow, 1989). Defined as [perimeter of ejecta] / SQRT(4·π·[area of ejecta]), which is effectively the percent difference of the perimeter of the flow vs. the perimeter of a perfect circle with the equivalent flow area. Unitless. Column format is variable-width, decimal to the hundredths place.

Note 1: The area of the crater itself IS included in this calculation.

Note 2: In this calculation, local spherical effects were NOT taken into account.

LAYER_[1, 2, 3, 4, 5]_EJECTARADIUS_EQUIV The radius to which the crater's

963 ejecta would extent if it were a circle with the same area as LAYER_[1, 2, 3,
964 4, 5]_AREA. Column format is variable-width, decimal to the hundredths place.
965 LAYER_[1, 2, 3, 4, 5]_EJECTARADIUS_RELATIVE The relative radius to which the
966 crater's ejecta would extent if it were a circle with the same area as LOBE_[1, 2,
967 3, 4, 5]_AREA. Calculated by:
968 LAYER_[1,2,3,4,5]_EJECTARADIUS_EQUIV / DIAMETER_CIRCLE_IMAGE.
969 Column format is variable-width, decimal to the hundredths place.
970 CRATER_NAME Drawn from the USGS's online Gazetteer of Planetary Nomenclature,
971 maintained by Jennifer Blue (http://planetarynames.wr.usgs.gov/). Column
972 format is variable-width string.
973

Appendix B –Uncertainties in Circle and Ellipse Fits

The human error in measuring craters followed a Gaussian distribution about the true rim for a crater of a given size as measured by the residuals from crater fits. This Gaussian was modeled from a sampling of ~40,000 craters via the following method: (1) After fitting a circle to a crater, the radial distance of each identified vertex was subtracted from the fitted circle radius. (2) The standard deviation of these residuals for each crater was calculated. (3) These standard deviations versus the crater diameter were fit to a power-law which modeled well the distribution, where the fit was of the form $\xi = y_0 + A \cdot x^p$ where ξ is the recorded value; y_0, A, and p are fit parameters; and x is the "true" location of the vertex. The fit parameters were calculated to be $y_0 = 0.015 \pm 0.001$, $A = 0.024 \pm 0.000$, and $p = 0.938 \pm 0.003$.

To understand the effects of this on the final crater database, an ideal circle of different diameters was modeled with each size having $2\pi D$ vertices. To the x and y value of each vertex, random noise drawn from the Gaussian distribution. For example, a D = 5 km crater was modeled to have a standard error in each vertex of ~±0.12 km. A Monte Carlo set of simulations both fitting a NLLS circle and ellipse to the model crater was run. The ratio of the fitted diameter versus the true diameter of the circle fit was recorded as was the ellipticity ε as a tracer of the uncertainty in the ellipse fit. This simulation was performed for 10,000 model craters each at diameters between 1.0 and ~53 km in multiplicative intervals of $2^{1/4}D$.

The mean and standard deviation of each simulation set of circle diameters were recorded and plotted against the true diameter (Fig. 2, top panel). A small aliasing of 0.4% was present at the smallest diameters: For D = 1 km, the Monte Carlo simulations show the NLSS fit is 100.4±3.2% of the true diameter with this noise model; it drops to <100.1% for $D \gtrsim 10$ km, and the $\mu \pm \sigma$ range of the fits was within the true diameter for all crater ranges examined. This is an over-estimate for most of the small craters since the majority of $D \sim 1$ km craters were identified in the final search at higher resolution. A comparable model run for the increased resolution of the final crater identification found similar results, with the $D = 1$ km value

100.3±2.8%.

The ellipticity ε should be 1.0 for all cases (a and b should be the same) if the fit were perfect and the noise level 0%. The mean and standard deviation of $\varepsilon(D)$ are shown in Fig. 2, bottom panel. ε fell below 1.1 for $D \gtrsim 1.5$ km, and it fell below the 1.05 level for $D \gtrsim 2.5$ km.

1005 Appendix C - Archetypal Examples of Crater Ejecta Morphologies

1006 This section contains archetypal examples of the crater ejecta morphologies that are
1007 included in this database in Figs. 9 and 10. Multiple examples of each type from the first two
1008 ejecta morphology columns are included (first column is basic type from *Barlow et al*. [2000];
1009 second column describes the texture and shape of the ejecta). Simple radial ejecta is not shown.

1010 Layered ejecta (LE) displays several morphologic sub-types that are used in its five-letter
1011 classification. The first is how many layers of ejecta are present – a single layer (SLE), two
1012 (double) layers (DLE), or three or more layers (MLE). The second type discriminator is if the
1013 ejecta terminates in a rampart or not, as indicated by an R or P (for "pancake") as the fourth
1014 letter. If *any* part of the ejecta edge displays a rampart morphology, even if the rest does not, the
1015 R designation is given in lieu of P in this catalog. Third is how the edge of the ejecta terminates,
1016 whether it is sinuous or fairly circular. The lobateness factor Γ is defined in Eq. 3. If $\Gamma \leq 1.5$,
1017 the ejecta is circular (*e.g.*, SLEPC). If $\Gamma > 1.5$, the ejecta is sinuous (*e.g.*, SLERS).

1018 *Barlow et al.* [2000] also recommended that when multiple types of ejecta are present
1019 around a single crater, the terms be combined. For example, a crater that displays one
1020 continuous layer of ejecta in addition to radial ejecta would be designated "SLERSRd." It is on
1021 this point that this database deviates from those recommendations. Instead, a backslash ("/") is
1022 used to indicate multiple classifications for multiple layers. This is done for expandability and to
1023 provide better information. For example, a class of craters found in the mid-northern latitudes is
1024 DLE, but the inner layer is PC while the outer is RS. Hence, this is designated as
1025 "DLEPC/DLERS" in this database. In another example, sometimes there will be a radial ejecta
1026 component between two cohesive ejecta layers. Pure radial non-cohesive ejecta is *not*
1027 considered a layer in the S/D/M classification, so in this case the designation would be
1028 "DLEPC/Rd/DLERS."

1029 The second ejecta morphology field describes the overall texture of the LE blanket and it
1030 provides additional information about its edge; this is found in `MORPHOLOGY_EJECTA_2` as a

two- or four-letter code. The first two letters are either "Hu" or "Sm" which stand for "hummocky" and "smooth" to describe how the ejecta blanket appears in THEMIS Daytime IR data. These two are always present in this column if there is a layer of ejecta present while there may or may not be an additional two letters used. If present, they are "BL," "SL," "Am," or "Sp." These stand for "broad lobes," "small lobes," "amorphous," and "splash." "Broad lobe" is used when the separation between different lobes of a layer is more than 50% of the extent of the layer; this is measured by eye and is not an exact delineation. "Small lobe" is where the terminus of the ejecta is more of a serrated "crinkle scissor" type, though it is more precisely defined as when the separation between these serrations does not extend more than 50% of the extent of the ejecta (this is also not exact). The "amorphous" type is for an overall ejecta that is generally asymmetric and lacks any defined shape. "Splash" is when the ejecta appears as a splash onto the surface, generally extending far from the crater rim but separated into many different strands.

A final third column `MORPHOLOGY_EJECTA_3` was occasionally used to describe unique shapes of ejecta blankets. These types are: Butterfly, Rectangular, Splash (redundant from above), Bumblebee, and Pin-Cushion. In addition to these, "Pseudo-Butterfly" and "Pseudo-Rectangular" are occasionally used to describe the ejecta around a single crater. Occasionally, a binary impact will occur and the two craters overlap, their touching rims being straight between the two. In this case, there may be cohesive ejecta that appears to be squeezed between the two in which case "bumblebee" is used for both craters. Finally, even if there is no ejecta but the crater is at the head of what on Earth would be considered a sandbar, the term "Sandbar" is placed in this column of morphology.

Butterfly ejecta occurs around a fairly elliptical crater. This ejecta will have a zone of avoidance at the edge of the crater at one end of the major axis; this avoidance zone was found to typically cover. The ejecta has the farthest extent from the crater almost immediately past this zone, and it stays relatively far from the rim throughout most of the length of the crater. It will narrow as it approaches the other end of the major axis and have nearly a similar zone of avoidance, though it will still be present in a substantially reduced extent. It will typically have

one or two "tendrils" extending beyond this. If the ejecta is similar but does not, for example, nearly disappear at the other end of the major axis, or if the ejecta does not have an obvious farthest extent immediately past the zone of avoidance, the ejecta is considered "Pseudo-Butterfly." Eighty-four craters were classified as having butterfly ejecta, while 125 were classified as pseudo-butterfly.

Rectangular ejecta may have a similar genesis to the Butterfly type, but it has a nearly 180° zone of avoidance at both ends of the major axis, and it will extend a nearly constant distance from the crater's edge along the rest of the crater. The Splash type is the same as the "Sp" suffix in the second morphology classification. Pin-Cushion ejecta is exclusive to the ---PC (first morphology column) and Hu (second morphology column) type. In the THEMIS Daytime IR mosaics, this crater appears to be bulbous with a pitted texture, appearing at the THEMIS 100 m/pix data to resemble a pin cushion. This may be due to overlying radial ejecta as this often had a `MORPHOLOGY_EJECTA_1` classification of "Rd/SLEPC," although this only became apparent at the higher 100 m/pix data and was not clear in the 230 m/pix mosaics.

Table 1: Schema used to define preservation states ("class") for craters. Craters are classified with three morphologic characteristics and the relative depth from topography (if available). The corresponding rank is converted to a preservation class. The majority of craters in a given class will have characteristics from that row, but that is not always the case. It is possible - if highly unlikely - for a crater to have, for example, a "Sharp" rim while having no ejecta and being mostly infilled.

Relative Depth	Rim	Ejecta	Interior	Rank[3]	Class
<1/4 (1)	Rimless (1)	None (1)	Mostly Infilled / Highly Modified[1] (1)	4-6 (3-4)	1
¼-1/2 (2)	Slightly Elevated (2)	None (1)	Significant Deposits / Modification[1] (2)	7-9 (5-6)	2
½-3/4 (3)	Some Degradation / Modification[1] (3)	Some Erosion / Modification (2)	Some Infilling / Modification[1] (3)	10-13 (7-9)	3
>3/4 (4)	Sharp[2] (4)	Pristine (3)	Pristine (4)	14-16 (10-11)	4

[1]Modification includes: Gullying/dissection, fracturing, lava flows, ice flows, mass wasting (*e.g.*, from the rim), superimposed cratering, etc.

[2]Does not necessarily mean "pristine" (*i.e.*, can have a small crater superimposed or a very small bit of modification).

[3]Parenthetical values are if depth information is not present.

1085 Table 2: Craters and properties of the craters used in studying the fractal nature of ejecta.

Crater ID	Diameter	Latitude	Longitude	Ejecta Type 1	Ejecta Type 2
15-000458	6.1 km	4.3°	138.2°	SLEPC	HuSL
08-000295	8.2 km	5.0°	-152.7°	SLERS	HuBL
06-000263	10.4 km	30.3°	108.0°	SLEPC	Hu
14-000259	18.0 km	5.4°	102.4°	MLERS[1]	HuBL

1086 [1]Outer ejecta layer was analyzed.

1087

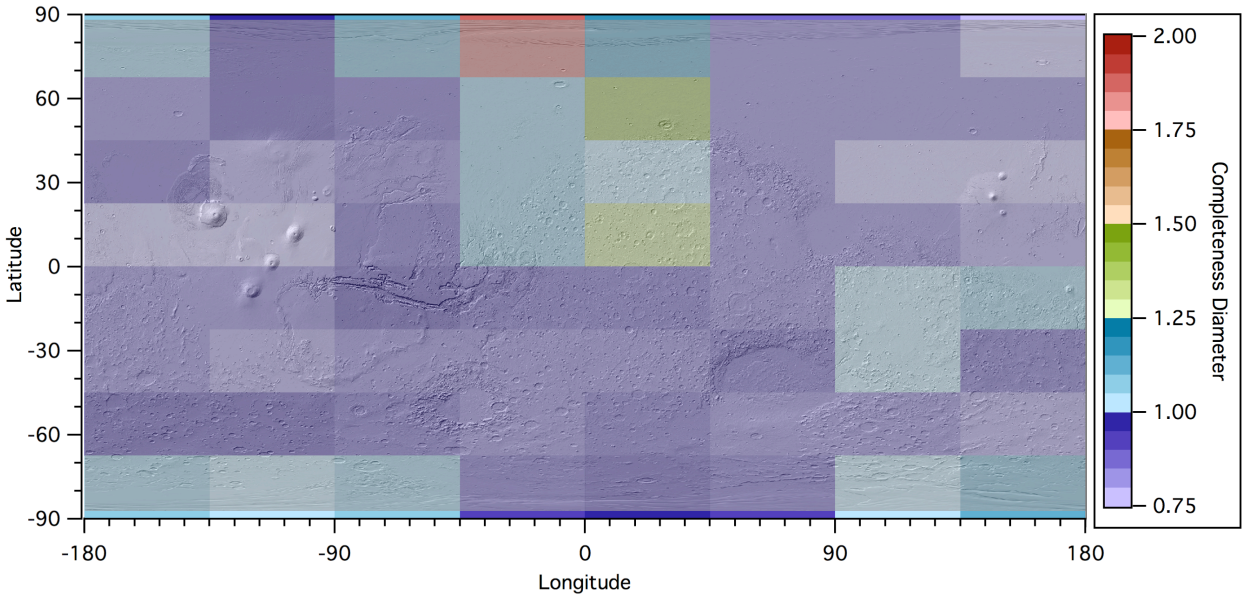

Figure 1: Color-coded area plot showing statistical completeness of crater diameters across the planet (see Section 7.1). Bins are 22.5° latitude by 45° longitude resolution. Finer resolution gives skewed results near the poles due to small number statistics. The low completeness in the bin centered at 78.75°N, -22.5°E is due to the young, large Lomonosov impact crater and the north polar cap, and the one centered at 56.25°N, 22.5°E is due to the similarly young, large Lyot impact crater. This is discussed further in Section 7.1.

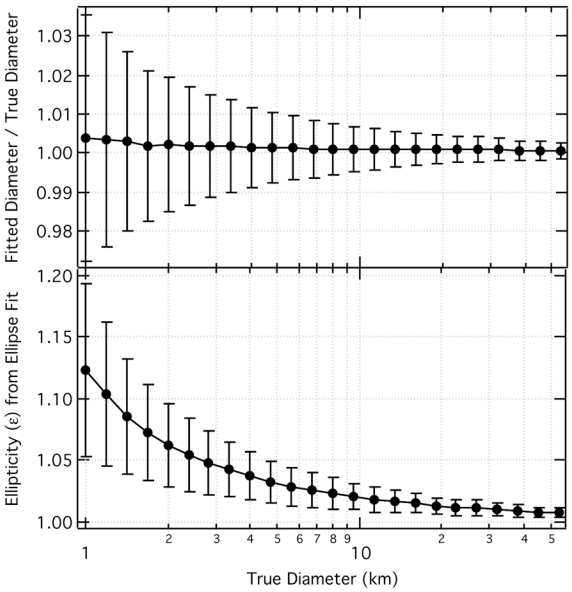

Figure 2**:** Both panels show the results of Monte Carlo simulations using the NLLS circle and ellipse on a "noisy" circular crater model. Ten thousand simulations for each diameter point were conducted (1.0-53 km in $2^{1/4}D$ multiplicative intervals), and the mean and standard deviation of the results are shown (at larger diameters, error bars are smaller than the symbol size). Top - Deviation of the circle-fit diameter from the true model diameter, where 1.00 would be a perfect match. Bottom - ε, which should be 1.00 for the modeled circle.

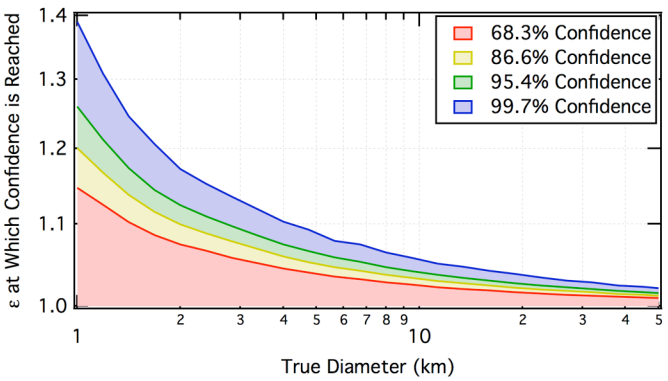

1104

1105 Figure 3**:** For the uncertainty model described in the text, the shaded regions represent all ε at
1106 which the confidence that the fitted ε is a true representation of the crater's ε for a given
1107 confidence level. For example, if one wanted to state with 95.4% confidence (2σ) that a $D = 2$
1108 km crater had a certain ε value, they could only do so for $\varepsilon > 1.12$ from this database.

1109

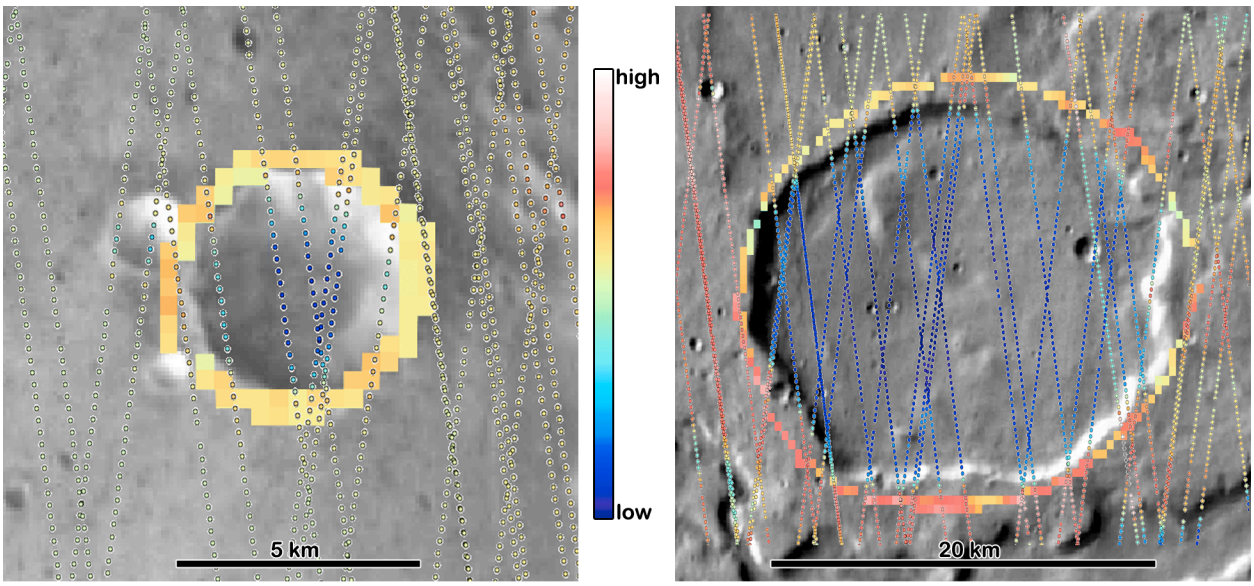

Figure 4**:** Images showing two craters with MOLA PEDR and MEGDR data overlaid. Left crater is D = 5.8 km (-1.5°N, 102.1°E) and right crater is D = 21.1 km (-40.1°N, 173.5°E). The background image is THEMIS Daytime IR mosaic. Colored squares around the rim are the MEGDR data that were used to define the rim height in the main topographic analysis. Smaller colored circles show the PEDR tracks. Where a circle does not overlap a square, the MEGDR data point had no actual data and was purely interpolated. All PEDR points are shown, but only those that were within two THEMIS pixels of the crater rim were used in the comparison analysis in this section.

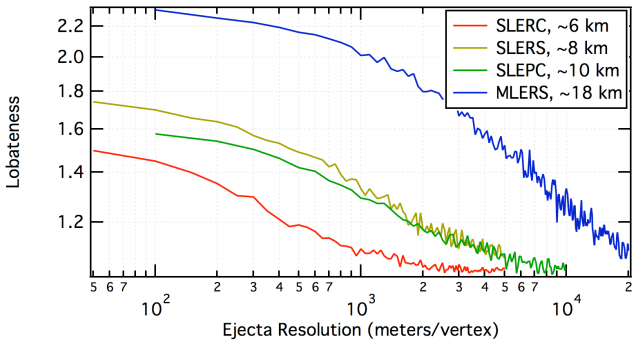

1120

1121 Figure 5**:** Effect of different resolutions for different crater ejecta morphologies on the derived
1122 lobateness. Each type behaves differently as measured by the slope and shape of the curve.
1123 Resolution was reduced until there were 10-20 vertices that defined the ejecta perimeter.

1124

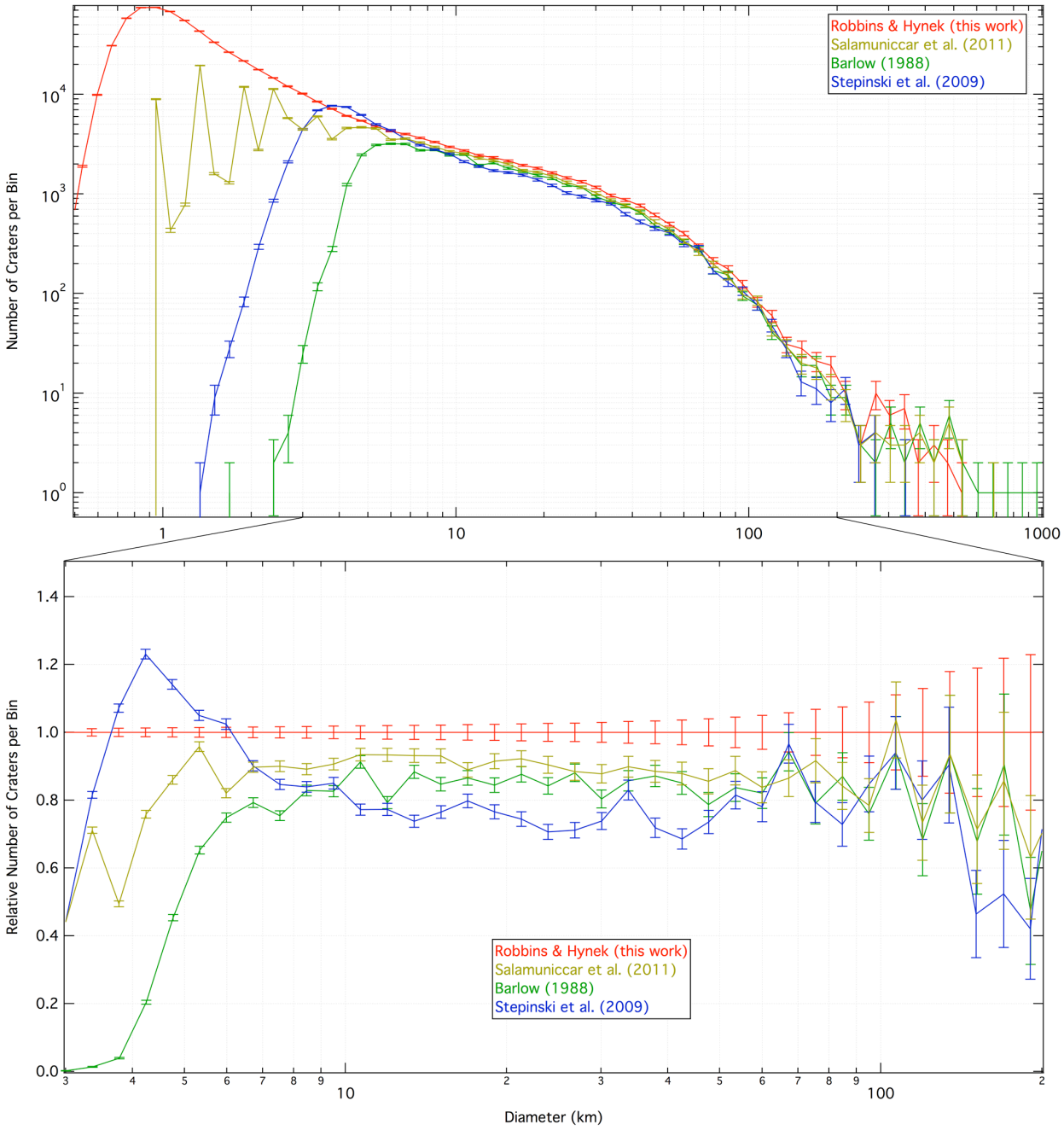

Figure 6**:** Comparison between four global Martian crater databases with craters binned in $2^{1/6}D$ intervals. The original Barlow database is not complete to D = 5 km, though the current in progress version is closer to this work. The Stepinski database displays a marked increase in craters 3 < D < 7 km, the likely reason discussed in the text. Salamunićcar database relative to this shows good agreement until diameters D < ~6 are reached, at which point their diameters are posterized as discussed in the text. Top - Incremental size-frequency distributions over all ranges included in each database. Note the released database will only contain $D \geq 1$ km craters.

Bottom - Ratio of incremental size-frequency distributions relative to the database in this paper. Error bars were calculated by the square-root of the counts in the incremental size-frequency bin divided by the counts in the bin for this database. Note the diameter range is a sub-set of the top panel.

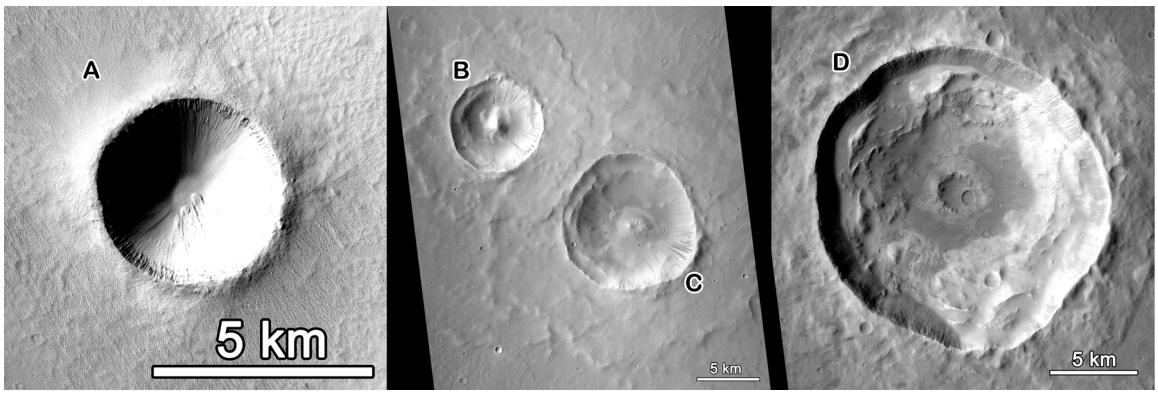

Figure 7: Basic crater morphologies used in the first morphology column; scale bar is 5 km in all examples. Imagery is from CTX [*Malin et al*., 2007]. (A) is a basic simple crater with some "slump deposits" along the southeast side (CTX image P19_008619_1840_XI_04N152W). (B) is a complex, central peak crater, while (C) is a complex summit pit crater; both have terraced walls (CTX image B02_010379_1846_XN_04N325W). (D) is a larger complex crater with a central pit and wall terraces; it also has some "slump deposits" from the walls onto the floor of the crater (CTX image B02_010554_ 1869_XN_06N063W).

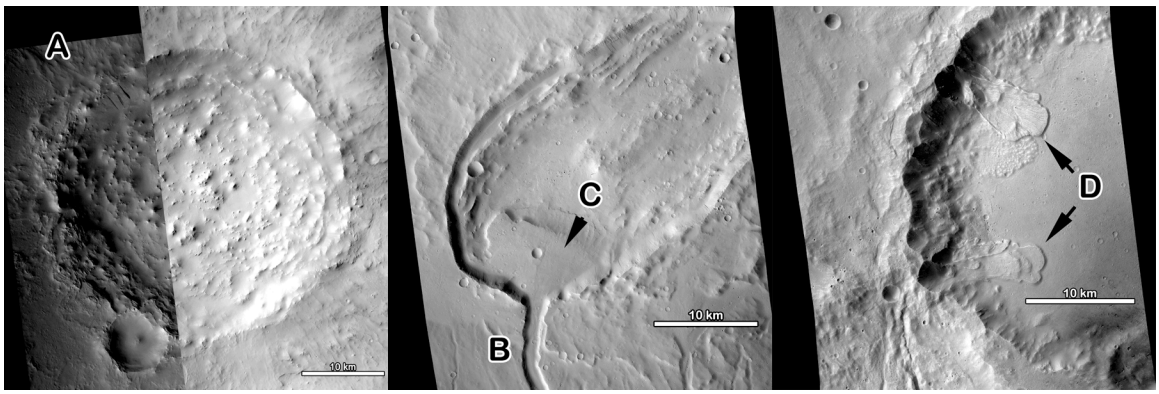

Figure 8: Select floor and wall morphologies; scale bar is 10 km in all examples. Imagery is from CTX. (A) is a crater floor with heavy deposits ("floor deposits" in the third column) that would have a first morphology column label of CpxUnc (complex, unclassifiable) (CTX mosaic from P07_003799_1961_XN_16N311W and P19_008282_1982_XN_18N311W). An example of a channel breaching the crater wall is (B) and (C) is "valley deposits" on the crater floor of Rahe Crater (CTX image B04_011399_2045_XN_24MN097). (D) shows an example of "landslide deposits" (CTX image G02_018952_1919_XI_11N021W).

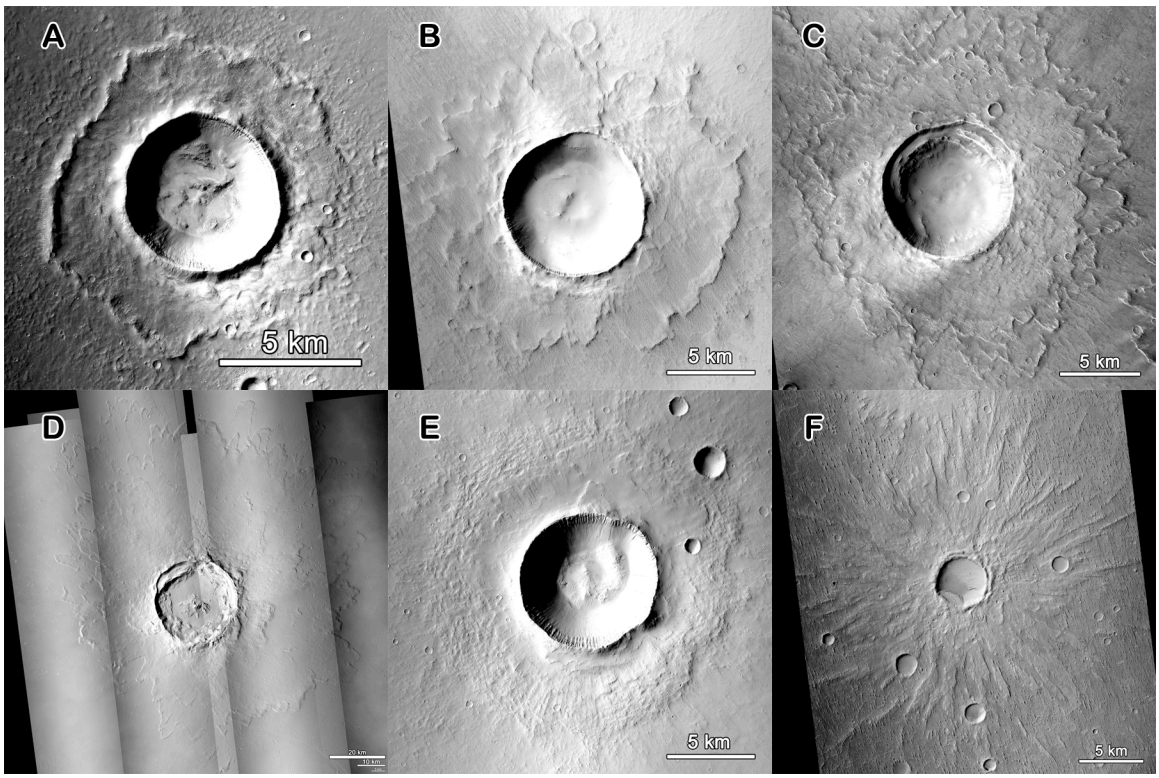

Figure 9: Select ejecta morphologies; scale bar is 5 km in all cases except (D), where the largest bar is 20 km. (A) is an example of the SLERC type in the first morphology column and HuSL (hummocky, short lobes) for the second (CTX image P21_009439_1850_XN_05N221W). (B) is an SLERS, SmSL (smooth, short lobes) (CTX image P19_008619_1840_XI_04N152W). (C) is a DLERS, HuSL type (CTX image B03_010694_1868_XI_06N285W). (D) is the MLERS, HuBL type (CTX mosaic from many images). (E) is an example of the "Pin-Cushion" morphology (also SLEPC, Hu) which, at the higher CTX resolution, has a strong radial ejecta component overlying the cohesive layer (CTX image P21_009381_2010_XN_21N080W). (F) is a good example of the SLEPS, HuSp type (CTX image P17_007606_1808_XI_00N210W).

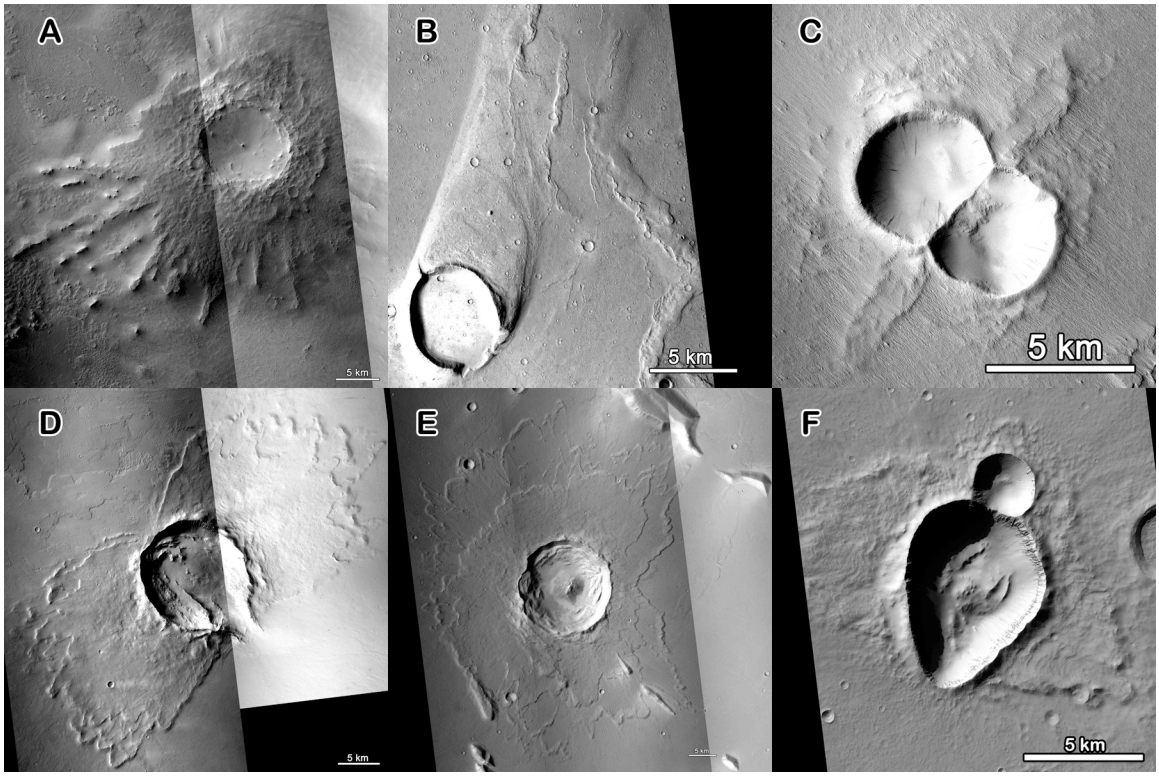

Figure 10: Select ejecta morphologies; scale bar is 5 km in all examples. (A) is both an SLEPd (pedestal crater), an example of the HuSp (hummocky, splash) type, and "Splash" in the third ejecta morphology column (CTX mosaic from P13_005942_1816_XI_01N135W, P21_009304_1806_XN_00N136W, P22_009515_1806_XI_00N136W.IMG). While not actually ejecta, "Sandbar" was indicated in the third ejecta morphology column for craters such as (B) (CTX image P03_002392_1948_XN_14N058W). (C) is the bumblebee ejecta type from a binary impact (CTX image P15_006971_1842_XN_04N151W). (D) is a DLERS, SmBL type with "Butterfly" in the third ejecta morphology column (CTX mosaic from P12_005874_1916_XN_11N080W and P20_008880_1915_XN_11N080W). (E) is the "pseudo-butterfly" type (also DLERS, SmBL) because, while it has the zone of avoidance to the east and some of the larger ejecta mobility immediately beyond the zone of avoidance, it continues around to the west as the normal DLE ejecta type and does not come back to the crater rim as with (D) (CTX mosaic from P02_001962_1967_XN_16N199W, P13_006142_1964_XN_16N198W, P20_008792_1980_XN_ 18N199W). (F) is an example of the "Rectangular" type which, while likely a progression from "Butterfly," has a ~180° zone of avoidance at the ends of the major axis. (CTX image B18_016578_ 1475_XI_32S359W).